Evidence for Bathymetric Control on Body Wave Microseism Generation

Garrett G. Euler[1,*], Douglas A. Wiens[1], and Andrew A. Nyblade[2]

March 1, 2013

For Submission to
Journal of Geophysical Research

*Correspondence: ggeuler@seismo.wustl.edu

[1]Department of Earth and Planetary Sciences, Washington University in St. Louis, Campus Box 1169, One Brookings Drive, St. Louis, MO 63130-4862, USA

[2]Department of Geosciences , Penn State , 441 Deike Building , University Park, PA 16802, USA

Abstract

Microseisms are the background vibrations recorded by seismometers predominately driven by the interaction of ocean waves with the solid Earth. Locating the sources of microseisms improves our understanding of the range of conditions under which they are generated and has implications on seismic tomography and climate studies. In this study, we detect source locations of compressional body wave microseisms at periods of 5-10s (0.1-0.2Hz) using broadband array noise correlation techniques and frequency-slowness analysis. Data include vertical component records from 4 temporary seismic arrays in equatorial and southern Africa with a total of 163 broadband stations and deployed over a span of 13 years (1994 to 2007). While none of the arrays were deployed contemporaneously, we find the recorded microseismic P-waves originate from common, distant oceanic locations that vary seasonally in proportion with the amount of extratropical cyclone activity in those regions. We do not observe consistent sources of microseismic PP and PKP waves in our analysis, possibly as a result limited detection due to the higher attenuation of those phases. We do observe that the interference of ocean swell at low latitudes is not a significant source of microseismic P-waves as most of our identified source locations are found within the high-latitude extratropical cyclone belts in the northern and southern hemispheres. Furthermore, we show that the influence of bathymetry and wave activity on the generation of body wave microseisms is apparent from the distribution of microseisms originating from features in the North Atlantic (along Retkjanes Ridge, southeast of Greenland, and northeast of Iceland) as well as in the southern ocean (South Georgia Island, the Antarctic Peninsula, the South Atlantic triple junction, the Rio Grande Rise - Walvis Ridge system, the Conrad Rise, and the Kerguelen Plateau). These observations corroborate double-frequency microseism theory and suggest that computation of ocean wavenumber spectra for microseism-based climate studies may not be necessary. As expected

from double-frequency microseism theory, we observe variations in source location with frequency: evidence that tomographic studies including microseismic body waves will benefit from analyzing multiple frequency bands.

1. Introduction

Recognition that microseisms provide information useful for site selection [e.g., Peterson, 1993; McNamara and Buland, 2004], imaging Earth structure [Sabra et al., 2005; Bensen et al., 2007; Yang and Ritzwoller, 2008; Lin et al., 2008, 2009; Prieto et al., 2009; Tsai, 2009; Harmon et al., 2010; Zhang et al., 2010b; Lawrence and Prieto, 2011; Lin et al., 2011, 2012a,b], and monitoring geologic structures [Sens-Schönfelder and Wegler, 2006; Wegler and Sens-Schönfelder, 2007; Brenguier et al., 2008a,b] and climate [Aster et al., 2008, 2010; Stutzmann et al., 2009; Grob et al., 2011] are the primary motivations in studying these more exotic sources. While some microseism studies use single-station techniques [e.g., Stutzmann et al., 2009; Obrebski et al., 2012], the use of an array of seismometers to filter the wave energy by slowness (the inverse of velocity), azimuth and frequency [Burg, 1964; Capon, 1969; Lacoss et al., 1969; Rost and Thomas, 2002, 2009] is a more powerful approach. Array analysis of microseism properties has focused on surface wave sources [Ramirez, 1940a,b; Haubrich and McCamy, 1969; Capon, 1973; Cessaro and Chan, 1989; Cessaro, 1994; Friedrich et al., 1998; Schulte-Pelkum, 2004; Shapiro et al., 2006; Stehly et al., 2006; Chevrot et al., 2007; Obrebski et al., 2012] and compressional body wave sources [Toksoz and Lacoss, 1968; Haubrich and McCamy, 1969; Gerstoft et al., 2006, 2008; Koper and de Foy, 2008; Zhang et al., 2009; Koper et al., 2009, 2010; Landes et al., 2010; Zhang et al., 2010a]. In general, these studies have found that surface wave microseisms observed on continents are primarily generated from ocean wave action near coastlines while body wave microseisms are typically generated near the wind source. This

distinction leads to large differences in the source locations of the two wave types as ocean waves may travel thousands of kilometers from the storm center (the wind source) to a coastline.

Microseisms created by the action of ocean waves produce two broad peaks in the Earth's background spectra and are classified as either single-frequency (SF) or double-frequency (DF) microseisms depending on the mechanism of generation [Longuet-Higgins, 1950; Haubrich et al., 1963; Hasselmann, 1963; Webb, 1992; Bromirski and Duennebier, 2002; Tanimoto, 2007; Webb, 2008]. While both SF and DF surface wave microseisms are regularly observed, only DF body wave microseisms have been conclusively detected [e.g., Haubrich and McCamy, 1969] although a recent effort to detect teleseismic body waves in the frequency range of SF microseisms has been made [Landes et al., 2010]. Recent studies [Bromirski et al., 2005; Tanimoto, 2007; Zhang et al., 2010a] have further differentiated the DF microseisms into two sub-classes: long-period double-frequency (LPDF) and short-period double-frequency (SPDF). This further division arises because the source locations of these two sub-classes are often distinct, apparently due to the greater attenuation of ocean swell from distant storms at SPDF frequencies than at LPDF frequencies. The increased attenuation of higher frequency ocean waves also gives rise to a stronger correlation of SPDF microseisms with wind activity near the source location [Bromirski et al., 2005; Zhang et al., 2009].

Within a few years of first identification [Backus et al., 1964], studies found that microseismic P-waves predominately originated near storms over the ocean and often from storms moving faster than the storm-wind generated ocean waves [Toksoz and Lacoss, 1968; Lacoss et al., 1969; Haubrich and McCamy, 1969]. After 3 decades with little further study, interest in microseismic P-waves returned [e.g., Gerstoft et al., 2006] as tomographic imaging with Rayleigh wave microseisms became routine practice [e.g., Benson et al., 2007]. The identification of microseismic body waves generated from distant storms that penetrate the

Earth's core has been recently reported numerous times [Gerstoft et al., 2008; Koper and de Foy, 2008; Koper et al., 2009, 2010; Landes et al., 2010]. Several studies have also noted that long-term averages of microseism data from arrays in North America and Asia identify sources of compressional body wave microseisms coming from regions of increased ocean wave activity [Gerstoft et al., 2008; Zhang et al., 2010a; Landes et al., 2010], suggesting that climatic signals are recoverable from the analysis of the body wave microseism spectrum. In this study, we infer the seasonal distribution of microseismic body waves propagating through several regional broadband arrays in equatorial and southern Africa utilizing noise correlation techniques and frequency-slowness analysis. Our focus is on the properties of compressional body wave microseism sources in two period bands: a SPDF band (5-7.5s) and a LPDF band (7.5-10s). We find evidence for several common, stable locations in the Southern Ocean supporting that body wave microseisms produced by the interaction of opposing ocean wave fields are enhanced by bathymetry [Longuet-Higgens, 1950; Tanimoto, 2007; Kedar et al., 2008; Ardhuin et al., 2011].

2. Data

Observations of compressional body wave microseisms have used arrays in North America [Toksoz and Lacoss, 1968; Haubrich and McCamy, 1969; Lacoss et al., 1969; Gerstoft et al., 2006, 2008; Koper et al., 2009; Zhang et al., 2009, 2010b], Asia [Koper and de Foy, 2008] or on both continents [Zhang et al., 2010a; Landes et al., 2010] with one notable exception at short periods [Koper et al., 2010]. We chose to use 4 arrays deployed in the equatorial and southern regions over a 13 year time span (Figure 1) to understand the characteristics of compressional body wave microseisms in Africa. For the remainder of this study we refer to the arrays as the Cameroon, Ethiopia, South Africa and Tanzania arrays when we need to distinguish between them. In the following sections we provide a short description of each array.

2.1 Tanzania

The Tanzania Broadband Seismic Experiment has the fewest seismometers, the shortest duration, and the earliest deployment of the arrays in our study. The array consists of 21 broadband stations deployed from May 1994 to June 1995 in two lines forming a cross pattern intersecting near the middle. The linear components have 11 seismic stations spaced about 100km apart with one line oriented roughly east-west and the other northeast-southwest. The seismic equipment consisted of a Streckeisen STS-2 or Guralp CMG-3ESP seismometer linked to a Reftek RT72A-08 digital recorder sampling at 20Hz and 1Hz. The experiment has been utilized in imaging the structure of the Archean Tanzania Craton and the terminus of the East African Rift in northern Tanzania using local, regional, and teleseismic earthquakes [e.g., Nyblade et al., 1996; Weeraratne et al., 2003; Julià et al., 2005].

2.2 South Africa

The Southern Africa Broadband Seismic Experiment is the most instrumented array in our study with 82 broadband sites deployed from April 1997 to July 1999. The array has been successfully used to image the Archean Kaapvaal and Zimbabwe Cratons, the surrounding Proterozoic provinces, and the underlying mantle using teleseismic earthquakes and seismic noise [e.g., James et al., 2001, 2003; Fouch et al., 2004; Yang et al., 2008]. The array was comprised of 32 fixed stations and a 23 station mobile component that occupied another 50 sites over the 2-year deployment. The sites were spaced at roughly 100 km intervals in a fairly regular grid with lines oriented North-South and East-West and a total aperture of approximately 2000km in the northeast-southwest direction and 700km in northwest-southeast direction. Instrumentation included Streckeisen STS-2 and Guralp CMG-3 seismometers digitized at 20Hz

which was decimated to 1Hz for our analysis.

2.3 Ethiopia

The Ethiopia Broadband Seismic Experiment utilized 38 broadband stations deployed between March 2000 and March 2002. Data from the array has imaged the crustal and upper mantle structure of the East African Rift and surrounding plateaus using local, regional, and teleseismic earthquakes and seismic noise [Nyblade and Langston, 2002; Dugda et al., 2005; Bastow et al., 2008; Kim et al., 2012]. We removed 10 stations from the original 38 station Ethiopia array as these sites formed a separate sub-array located 700km to the south in Kenya. During the first year of the experiment only 6 seismic stations were operational in Ethiopia while an additional 22 stations were installed in the region for the second year. The aperture of the Ethiopia array was about 550 km East-West and 700 km North-South with an irregular spacing of 50 to 200 km to optimize 3D seismic imaging at mantle depths. Stations were comprised of either a Guralp CMG-3, CMG-3T, CMG-40T or Streckeisen STS-2 seismometer that was digitally recorded at 20Hz and 1Hz.

2.4 Cameroon

The Cameroon Broadband Seismic Experiment was deployed between January 2005 to January 2007 with a design goal of 3D imaging the structure of the continental portion of the Cameroon Volcanic Line and the northern limit of the Congo Craton using teleseismic earthquakes [Reusch et al., 2010; Tokam et al., 2010; Reusch et al., 2011; Koch et al., 2012]. The experiment started with 8 pilot stations for the first year and was expanded to 32 stations for the remaining year. The array aperture varied from a maximum of over 1000 km in the northeast-southwest direction to a minimum of just over 600 km in the northwest-southeast

direction. The stations extend throughout the country of Cameroon and were spaced unevenly at 50 to 200 km intervals to optimize imaging at mantle depths using body waves and surface waves. Each station was composed of a Streckeisen STS-2, Guralp CMG-3T, or Guralp CMG-3ESP with a Reftek RT130 digital recorder sampling at 40Hz and 1Hz.

3. Methods

3.1 Isolation of Microseisms

Studying the seasonal characteristics of seismic noise requires the computationally difficult task of correlating months-long seismic records to produce noise correlation functions (NCFs) that summarize the spatially coherent noise field between pairs of stations. Previous studies have noted the equivalence of NCFs from correlating long time sections with those produced by averaging the correlations of smaller time sections [e.g., Bensen et al., 2007; Seats et al., 2012], a power spectum feature originally noted by Welch [1967]. We take advantage of this approach by dividing 1Hz vertical component recordings into 25-hour windows with overlap during the first hour of each day. This provides a seamless correlation of data across day boundaries with only minor data repetition. A side-effect of using time windows of this length is that most windows include earthquake waveforms that may bias the results. To suppress the earthquake waveforms in the records we utilize techniques intended for ambient noise tomography [Bensen et al., 2007]. Other studies average correlations of shorter time windows to suppress earthquakes [e.g., Gerstoft and Tanimoto, 2007]. For convenience, we summarize below the additional data processing on individual records in our study.

After windowing, records with no amplitude variation or those with data from less than 75% of the 25-hour window were removed to avoid bias from significant instrumental problems. The records were then detrended, tapered and converted to displacement. Next, both time-

domain and frequency-domain normalization was implemented to force the energy ratio of earthquake waveforms and microseisms to the relative proportion the two represent in time. In our study region and for all previous studies of microseisms that we are aware of, time periods with only microseismic noise far outnumber those with earthquakes waveforms. In this way, normalization leads to earthquake energy having little influence on the seismic noise field [e.g., Toksoz and Lacoss, 1968]. Our temporal normalization utilized a 2-pass sliding absolute mean. The first pass normalization utilized a 75s sliding window of the unfiltered records to suppress the effect of automatic re-centering of seismometer masses. The second pass normalization was tuned to the earthquake band (15s-100s) as in Bensen et al. [2007]. The last normalization step, spectral whitening, was implemented by dividing the complex spectra with a smoothed version of the amplitude spectra generated with a 2mHz-wide sliding mean. The normalized records were then cross-correlated for each unique station pair in every 25-hour window. These correlograms were cut between -4000s and 4000s in lag time to save space without affecting the coherent power between the stations. Finally, the NCF data was generated by stacking correlograms for each station pair across each month independent of year. For example, a January stack for a station pair in the Cameroon array may include correlations from January of 2005, 2006 and 2007. In Figure 2 we show NCFs from stacking correlograms for the entire deployment time of the Ethiopia array as the body wave microseisms, which travel at lower slownesses than surface wave microseisms, are visible at lag times corresponding to slownesses below 9s/º.

3.2 Frequency-Slowness Spectra

To understand the seasonal properties of microseisms propagating through each array, we used a conventional frequency-wavenumber (f-k) approach to estimate the frequency-slowness

power spectrum (hereafter referred to as the f-s spectrum) [Lacoss et al., 1969]. The f-s spectrum gives the distribution of wave power as a function of frequency, slowness, and direction of propagation through an array. This approach assumes the wave field is both stationary in space and time implying that the second-order statistics do not vary significantly for a set of our 25-hour recordings of an array. We expect this assumption is valid as the individual arrays in this study do not span one or more continents or include ocean-bottom stations and so the microseisms are unlikely to attenuate significantly across an array nor differ significantly in their characteristics. In the conventional approach, the f-s spectrum is estimated by frequency-domain delay and sum of cross power-spectra over a range of slowness vectors. The power of the array for an individual slowness and frequency is expressed as:

$$P(f,\boldsymbol{s})=\frac{1}{N^2}\sum_{i=1}^{N}\sum_{j=1}^{N} w_i' w_j C_{ij}(f)\,\mathrm{e}^{-i2\pi f \boldsymbol{s}(x_j-x_i)} \tag{1}$$

where w_i and w_j are station weights, C_{ij} is the cross spectra between stations i and j, s is the slowness vector in the direction of the wave source, and x_j-x_i is the spatial difference vector for the station pair. The ' symbol denotes complex conjugation. We normalize the cross spectra using each record's power spectra to give the coherency of the wavefield between a pair of stations at a particular frequency:

$$C_{ij}(f)=\frac{S_i'(f)S_j(f)}{\sqrt{S_i'(f)S_i(f)+S_j'(f)S_j(f)}} \quad . \tag{2}$$

Because correlograms are the time-domain representation of the cross power spectrum between a pair of stations, converting our NCFs to the frequency-domain gives the individual elements of the cross-spectral matrix **C**. We limited our NCFs to unique station pairs and did not include autocorrelations which means our estimation of the f-s spectrum is reduced to a summation over half of the off diagonal elements of **C**. This modifies (1) to a summation over pair indices rather than station indices:

$$P(f,\boldsymbol{s})=\frac{1}{N}\sum_{p=1}^{N} w_p \frac{C_p(f)}{|C_p(f)|}\mathrm{e}^{-i2\pi f \boldsymbol{s}\boldsymbol{x}_p} \quad . \tag{3}$$

where we have also combined the individual station weight and location terms. This reformulation halves the slowness spectrum computation while improving the beam resolution [Westwood, 1992]. A disadvantage of this approach is it prevents us from using more sophisticated high-resolution power spectra estimations that require inversion of the cross-spectral matrix [e.g., Capon, 1969] but these have been shown to give similar results to the conventional approach for statistical studies of microseisms [Koper et al., 2010].

We average over frequency to simplify our analysis to SPDF and LPDF sources:

$$P_{SPDF}(\boldsymbol{s})=\frac{1}{M_1}\sum_{f=\frac{1}{7.5\mathrm{s}}}^{\frac{1}{5\mathrm{s}}} P(f,\boldsymbol{s}) \quad , \tag{4}$$

$$P_{LPDF}(\boldsymbol{s})=\frac{1}{M_2}\sum_{f=\frac{1}{10\mathrm{s}}}^{\frac{1}{7.5\mathrm{s}}} P(f,\boldsymbol{s}) \quad . \tag{5}$$

M_1 and M_2 are the number of discrete frequencies over which the f-s spectra is summed in the SPDF and LPDF bands, respectively. These two bands represent a large frequency range that potentially may hide narrow band microseism sources in lieu of those with a greater bandwidth. Equivalently, sources that are short-lived will also have less power in the spectra compared to those that are persistent throughout the time span of an individual spectrum (1 month). Therefore, our f-s spectrum estimates give the distribution of microseisms as a function of slowness, azimuth, and frequency where the power is a product of microseismic source coherency across the array, time persistence, and frequency bandwidth.

3.3 Backprojection of Frequency-Slowness Spectra

Every slowness in a f-s spectrum corresponds to a unique ray path and distance for each phase included in our analysis (Figure 3a-b). This allows backprojection of the f-s spectrum over

a range of slowness for a particular body wave phase to a range of distances [Haubrich and McCamy, 1969]. Some of the body wave energy at these slowness ranges will also propagate as phases other than P, PP & PKP, but these are not expected to be significant as pointed out by Gerstoft et al. [2008]. To convert the spectrum from slowness and azimuth to latitude and longitude, slownesses are matched to a ray path and distance using the 1D Earth model AK135 [Kennett et al., 1995]. Combining the distance with the azimuth gives an estimate of the originating location of the body wave energy relative to the array center. For example, we projected the f-s spectrum of the NCFs stacked over the entire deployment of the Ethiopia array (Figure 2) in the slowness ranges of P and PKP_{bc} as they do not overlap in distance and are expected to be higher in amplitude compared to the other phases in this study (Figure 3b-d). The projected Ethiopia f-s spectrum indicates that the North Atlantic between Greenland and Iceland is a significant source of P-waves as well as two other sources in the southern hemisphere. Hindcasts of significant ocean waveheights [Tolman, 2009] averaged over the same time span show two main belts of high seas caused by extratropical cyclones (Figure 3e) which overlap with the regions of high microseismic P-wave excitation in Ethiopia. This provides some confidence that the body waves are P-waves and not PP-waves as the backprojection of the f-s spectrum assuming PP-wave propagation suggests the 3 sources in the central Pacific Ocean where wave heights are comparably lower (not shown). Direct comparison to significant wave heights is not necessarily relevant though as DF microseisms are generated during the interference of ocean waves and are modulated by the ocean depth [Longuet-Higgins, 1950]. Modeling of the ocean wavenumber spectrum [Kedar et al., 2008; Ardhuin et al., 2011, 2012; Obrebski et al., 2012] provides a more appropriate tool for relating body wave microseisms propagating beneath an arrays to the activity of ocean waves and storms. In this study, we make inferences based on maps of significant wave height and bathymetric excitation as these do not

require estimation of the ocean wavenumber spectrum and provide a realization of the DF microseismic spectrum for the long time scales we are interested in assuming wave-wave interference in the ocean is sufficiently random.

3.4 Approach to Summarizing Microseism Sources

Because every array has a different response to propagating waves [Rost and Thomas, 2002], combining the f-s spectra from multiple arrays is not a straightforward task. Instead we created a graphical interface to allow an analyst to pick peaks in a spectrum. These picks provide a simple representation of the microseismic body waves traversing an array and we use them to combine and summarize the f-s spectra from all the arrays in order to to look for common sources. We selected as many peaks as necessary to represent the main features of the f-s spectrum (Figure 4). While this approach does introduce some subjectivity, we felt it the most pragmatic method to avoid the detrimental effects of slowness aliasing that would otherwise hinder a more automated analysis. Other studies analyzing more slowness spectra include only the maximum of each spectrum to similarly avoid bias from aliased features [e.g., Koper et al., 2009, 2010].

3.5 Correcting Backprojection Locations for 3D Structure

Location errors larger than the width of the continental shelf have the potential to significantly alter interpretation of microseism generation near distant coastlines. While there are a number of studies that have located microseismic body wave sources, none to our knowledge have attempted to estimate the effect of 3D seismic velocity structure on the apparent locations. Such an investigation is straightforward as methods have been devised for earthquake waveforms [e.g., Nolet, 2008]. We perform a simple investigation into the effect of 3D velocity

structure on our apparent source locations assuming the 3D structure of Crust2.0 [Bassin et al., 2000] and HMSL-P06 [Houser et al., 2008].

To find the effect of the 3D velocity heterogeneity, we first generate ray paths through the 1D mantle model AK135 between each station in the array and an apparent source location. We then accrue a travel time perturbation for each ray path using Fermat's principle [Nolet, 2008]. Perturbations due to ellipticity are also included [Kennett and Gudmundsson, 1996]. We then performed a linear least-squares fit to the travel-time perturbations for an array as a function of either North or East position. This gives the slowness bias of the 3D heterogeneity in terms of seconds per degree North and East. This bias is then removed from the original slowness measurement to get a corrected slowness. Backprojection of the new slowness gives a better estimate of the source location if the Earth structure is appropriately represented by the velocity models and assuming the bias factors do not change significantly over the scale lengths of the location correction.

3.6 Array Response Functions

An array's spatial arrangement has a substantial effect on the resolution of that array's f-s spectrum [e.g., Haubrich, 1968]. In an ideal case, to perfectly resolve the propagating waves under the array requires an infinite number of stations to completely sample the waves spatially. While all arrays are far from this ideal, some represent a pragmatic compromise in resolution for a significant reduction in number of stations. One of the best ways to understand how well an array may estimate the true microseism f-s spectrum is to compute the array response function (ARF) for a single plane wave:

$$ARF(f,\boldsymbol{s}) = \frac{1}{N}\sum_{p=1}^{N} w_p \mathrm{e}^{-i2\pi f(\boldsymbol{s}-\boldsymbol{s}_0)\boldsymbol{x}_p} \tag{6}$$

where (6) is equivalent to (1) when the cross spectral elements **C** are 1 and s_0 is the slowness

vector of the plane wave propagating through the array. The ARF shows the aliasing pattern (resolution) of the array for that wave. We computed the array response for waves incident on each array with a slowness of 0 s/º over the LPDF and SPDF frequency bands. The ARFs were computed at each of the discrete M_1 or M_2 frequencies in the frequency bands of (4) and (5). The averaging over frequency smears aliasing features known as grating lobes because the slowness of the lobes varies with frequency [Rost and Thomas, 2002]. In strong contrast to the grating lobes is the central peak corresponding to the correct slowness of the propagating wave. This feature is comparatively enhanced because its slowness does not change with frequency.

All of the arrays in our study have similar station spacing but the number of stations, their arrangement and the overall aperture vary. This results in distinct array responses (Figure 5a,b). The number of stations in an array affects the signal-to-noise ratio of the central lobe, the arrangement determines the grating lobe locations, and the aperture of an array is directly related to the sharpness of the central lobe [Rost and Thomas, 2002]. For example, the Tanzania array is a 21 station, cross-shaped array with a maximum aperture of 900km while the Ethiopia array consists of 28 clustered stations with a maximum aperture of 750km. Comparing the responses of the two arrays for the SPDF band (Figure 5a) shows that while the central lobe of the Tanzania array response is actually sharper due to the array's wider aperture, there is substantial anisotropy of the central lobe width due to the cross-shape of this array. The Ethiopia response has a well developed central peak with no significant grating lobes within 30sec/deg. The overall background level of the response is also higher for the Tanzania array due to the fewer number of stations (Ethiopia has 28 while Tanzania has 21). The longer period spectral band (Figure 4b) is similar to that at the short periods but the spectral features are enlarged as a array response scales linearly with 1/f. This has a result of moving the rather significant grating lobes in the ARF of the South African array farther from the central lobe at longer periods.

4. Results and Discussion

4.1 Backprojection Spectra and Resolution

Backprojection maps for January and June f-s spectra (Figure 6a,b) illustrate the seasonal differences of P-wave microseisms in the northern and southern hemispheres. In January (Figure 6a) every array detects microseisms that appear to originate in the North Atlantic region south of Iceland and west of Greenland (hereafter SI). An averaged significant wave height hindcast for the month of January, 2001 (Figure 7) shows the SI region is associated with consistently strong ocean wave activity. Another apparent source of January P-wave microseisms observed in Tanzania appears to be located in West Africa (Figure 6a). As atmospheric disturbances over land do not generate significant P-waves [Hasselmann, 1963] and low frequency cultural noise is rare and has not been observed at teleseismic distances [e.g., Sheen et al., 2009], we suggest these microseisms are most likely PP-waves from the SI region which bounce beneath West Africa. Two of the arrays (Cameroon and Tanzania) also confirm P-wave microseisms originating from near the northern coast of Iceland (NI). Figure 7 shows this region as near strong wave heights and it is reasonable to assume that the averaged significant wave height maps for January during the years these two arrays were deployed probably indicate similar levels of ocean wave activity in this region. We have not investigated the possibility that the NI location represents a common PP-wave bounce point from two distant sources but we argue that such an occurrence is unlikely because of the increased attenuation of PP-waves. There are also several apparent sources of P-wave microseisms in the southern oceans and one apparent Hawaii PKP_{bc} source observed by the arrays (Figure 6a) but as these are not detected by 2 or more arrays for the month of January their provenance is less certain and we will not discuss them further here. Consistent with extratropical cyclone activity in June, there are no P-wave microseism

sources in the northern hemisphere with one potential exception off the coast of Siberia detected by the Cameroon array (Figure 6b). This single observation is compelling as it may be informative on changes in the state of the sea ice at this location since the other 3 arrays were deployed years earlier than the Cameroon array. Comparison to sea ice concentration maps determined by the NSIDC (ftp://sidads.colorado.edu/DATASETS/NOAA/G02135/Jun/) confirms that this P-wave microseism source location corresponds to a region in the arctic that does have low sea ice concentration. The distinct lack of coherent P-wave microseism detections for the South Africa array in Figure 6b for either hemisphere suggests there is little consistent microseismic activity in the region during June. This observation though is in conflict with that of the other three arrays which detected several sources of P-wave microseisms. One of these regions is in the Indian Ocean near the coast of southeast Asia. The month of June is at the end of the monsoon season for southeast Asia but we do not observe a notable increase in the wave heights there compared to surrounding regions (Figure 7). Furthermore this region is not found to be a significant P-wave microseism source during other months (not shown). A possible explanation is that these microseisms are generated by the interference of swell reflected along these coastlines. The swells in this case would have traveled from the southern Indian ocean where they were generated by the extratropical cyclone activity that is relatively strong in June [Guo et al., 2009]. We have found no other P-wave microseism sources that require the interference of reflected swells from distant locations so we believe this interpretation to be tentative. Furthermore, we have not eliminated the possibility that these are actually the detection of earthquake activity such as an aftershock sequence but this explanation also appears unlikely as the arrays were not deployed contemporaneously. Both Ethiopia and Cameroon also detect P-waves from two other locations, both of which are in the southern hemisphere extratropical cyclone belt (Figure 6b). One of these locations is near the plate boundary triple-

junction in the South Atlantic (SATJ). The remote Bouvet island near this location is unlikely to generate the ocean wave interference necessary to significantly excite P-wave microseisms due to its small size. Another possible explanation for this source of microseisms is that storms travel faster in this region than in other parts of the storm belt. At a speed exceeding that of the swells, the extratropical cyclones generate a focused amount of wave interference. We are not aware of the validity of such an explanation for this region but it potentially may be investigated further using extratropical cyclone track data (e.g., http://data.giss.nasa.gov/stormtracks/). A more viable explanation is that the shallower bathymetry related to SATJ is enhancing the wave-interference coupling to the solid Earth. Longuet-Higgins' [1950] theory of microseism generation indicates that specific ocean depths can have a substantial effect on P-wave excitation (see their Figure 2). The other source of P-waves is near the Kerguelen plateau (KP). This region has been noted by other studies as a significant source of body wave microseisms [Gerstoft et al. 2008; Landes et al., 2010; Zhang et al., 2010a]. This particular location likely represents the scenario for high amounts of microseism generation: regular storm activity over the local seas, increased wave interference from reflection off of the islands' coastlines and the enhancing effect of shallow bathymetry due to the Kerguelen plateau.

The interpretation of backprojection f-s spectra is limited by the slowness resolution of the corresponding array. For example, if an array has a low resolution because of a small aperture then it is difficult or impossible to determine the number, location, and geometry of the microseism sources. Aliasing issues such as grating lobes can further exacerbate resolution issues. To understand the resolution of the arrays in this study, we computed multi-planewave ARFs for each array corresponding to P-waves originating from several oceanic locations. These were constructed by averaging the ARFs for the different locations and then backprojecting the result (Figures 8a,b). For the SPDF band of 5-7.5s (Figure 8a) all backprojection P-wave source

locations match the expected locations with no discernible aliasing at other locations. The South Africa array has such high resolution for the southern P-wave sources that the corresponding response is barely sampled by our 1º grid. This undersampling is simple to avoid but interpretation of high resolution spectra at a global scale can be challenging as small source regions are visually easy to miss. Another method is to lower the resolution by removing outer stations from the array to limit the aperture. Considering that the other 3 other arrays have less than half the number of stations and can clearly detect the synthetic sources at nearly a tenth of the computational expense, we suggest that this as a better approach for large arrays unless extreme precision in location is desired. At LPDF periods (Figure 8b), the backprojection f-s spectra illustrate that the slowness resolution of several arrays may be too low to resolve neighboring P-wave source locations. In this case the responses of the sources merge and appear as a single source around the average location. Only the South Africa array is able to accurately separate the two North Atlantic source locations in the LPDF band while the other 3 arrays inaccurately indicate Iceland as the source location. The Ethiopia array resolution is also nearly too low to distinguish even the southern hemisphere source locations while the South Africa array resolution is again nearly too high for our sampling of the spectrum. We can get an idea of the dimensions of a source region by comparing the resolution of the ARFs to the observed f-s spectra. For example, the South Atlantic source detected by the Cameroon and Ethiopia arrays (Figure 6b) is much broader than the resolution at this location for either array. This indicates that the P-waves are generated over a broad region centered on the plate boundary triple-junction.

4.2 Peak Picks

Overall, we picked 206 peaks in 96 f-s spectra (Table 1). While the SPDF and LPDF

bands had similar totals, the number of peaks picked varied by array. Both the Tanzania and Cameroon arrays had nearly equal amounts of microseism detections in the two bands while the Ethiopia array detected nearly twice the LPDF sources compared to SPDF sources and the South Africa array mostly detected SPDF sources. Comparison of the slownesses of the f-s spectra picks finds ample P- and/or PP-wave sources while PKP phases account for <10% of the spectrum (Figure 9a). This is consistent with relative amplitudes for these phases found by stacking many near-surface earthquakes [Astiz et al., 1996]. A histogram of the peak power relative to the median of the entire spectra for of the picks (Figure 9b) finds most of the peaks are only about 2dB above the median dB value of each f-s spectrum but some peaks are as high as 10dB.

Comparing the peak locations in slowness space is helpful to understand the usual mode and direction of body waves crossing the arrays (Figures 10a,b). Most of the arrays have consistent peak locations to the Northwest and to various southern azimuths corresponding to either P- or PP-waves. By backprojecting and combining all of the SPDF or LPDF array picks in the P-wave slowness range onto a single map, we show that the rather complicated peak distribution in slowness space is simplified to a few geographic source regions (Figures 11a,b). In the Northern hemisphere, the main sources regions are the mid-Atlantic ridge extending South from Iceland (SI), near the southern tip of Greenland, and the northern coast of Iceland (NI). In the Southern hemisphere the source regions are the Walvis Ridge - Rio Grand Rise system (WR-RGR), the Antarctic Peninsula coastline (APC), the Enderby Abyss southeast of the Conrad Rise (CR), the plate boundary triple-junction in the South Atlantic (SATJ), and the vicinity of South Georgia Island (SG) and the Kerguelen Plateau (KP). The open ocean source regions (e.g., WR-RGR, SATJ and CR) may be explained by enhanced microseism generation in comparison to the surrounding regions due to the bathymetry [e.g., Longuet-Higgins, 1950] although the lack of

detections of LPDF P-wave microseisms from two of these locations (WR-RGR and CR) is not in agreement with the expected increase in excitation from bathymetry. Alternative explanations for the lack of LPDF microseisms from these locations are related to consistent changes in storm speed and intensity as a function of position. For instance this lack of detection may indicate that the speed of the storm exceeds the speed of the swell at SPDF periods but not at LPDF periods or that there is a lack of long period ocean wave interference due to weaker storm systems. These are unlikely to explain the lack of LPDF P-waves from the CR region though as there are nearby source regions of LPDF P-wave microseisms at similar latitudes (e.g., SG, SATJ, and KP). Recent work by Tanimoto [2007] has found that the bathymetric excitation functions are substatially different from those proposed by Longuet-Higgins [1950]. We expect this may have influence on our interpretation here but we have not examined this further. The APC source region only appears at LPDF periods and is also inconsistent with the expected increase in bathymetric enhancement of microseism production at SPDF periods for this location.

The P-wave microseism detections originating from along the WR-RGR are a bit puzzling in that they are farther North than most of the southern hemisphere sources. There are some extratropical storm systems that pass near this latitude range of the South Atlantic but they are infrequent and typically occur in the southern hemisphere winter months. Figure 6a indicates P-wave energy propagating across the Ethiopia array originating from this region during January (summer for the southern hemisphere) while a hindcast from this same time frame (Figure 7) shows that the average significant wave heights over the region are among the lowest in the southern hemisphere. Our only explanation for the WR-RGR P-wave microseisms is that the coupling of interfering waves in the region to the solid Earth is significantly enhanced by the local bathymetry in comparison to the surrounding regions.

Extratropical cyclones are strongest during the winter season of the hemisphere in which

they are located. Comparison of the strength of the northern and southern hemisphere storm tracks shows that during the northern hemisphere winter the ratio is about unity while during the southern hemisphere winter the southern storm activity is about 4 times that of the north [e.g., Guo et al., 2009]. Our limited monthly P-wave microseism source count agrees with these ratios (Table 2). However, the serendipitous effect of array location, source geometry and choices in averaging are likely to have had a significant influence on the observed ratio in microseism sources. Regardless, more comprehensive studies of microseisms may provide an independent measure of the relative strength of storms over the northern and southern oceans as the level of storm activity directly modulates the ocean wave spectrum and in turn the microseism spectrum.

4.3 Where are the Short Distance Sources?

One particular feature of this study that we find puzzling is the lack of body wave microseism sources at distances less than 60º. This can be seen in Figure 9a as the rather significant difference in number of peaks picked at a slowness of 6s/º compared to 8s/º. Attenuation from the asthenosphere is not a reason for the lack of PP arrivals and P arrivals from shorter distances as the ray paths corresponding to slownesses below 10s/º extend into the lower mantle and thus do spend a significant amount of time in the asthenosphere. One potentially reason may be that the body waves propagating through the array from closer locations are poorly approximated by a plane wave and so their coherency is diminished in the f-s spectrum computation. Additionally, at closer ranges the slowness of a P-wave varies more significantly than at further distances which will also reduce the coherency in the f-s spectrum for regional arrays. Both of these could be avoided by beamforming directly for each location using delays based on the travel times to each receiver rather than using a plane wave approximation and backprojection of the result. A third effect, similar to the previous two, is lateral velocity

structure. This can introduce phase delays that diminish coherency and bias the backprojection. Furthermore the Tanzania and South Africa arrays are less effective in resolving body wave microseisms due to their unusual array responses (Figures 5a,b) so this could be a significant influence on the apparent lack of closer P-wave microseism sources as the arrays with more P-wave detections (Cameroon and Ethiopia) are further from the southern storm belt compared to the Tanzania and South Africa arrays.

4.4 Coastal Reflection or Open Ocean Swell Interference?

Body wave microseism generation is generally accepted to be from non-linear wave interference [Haubrich and McCamy, 1969; Gerstoft et al., 2006; Zhang et al., 2009, 2010a]. There are several main ways that ocean waves interact [Haubrich and McCamy, 1969, Ardhuin et al., 2011]: (1) reflection along the coasts, (2) interference directly under a storm, (3) in the wake of a storm, or (4) between 2 storms. Because the intensity of ocean waves is strongest directly under a storm or nearby, the strongest sources of microseismic body waves are likely to be near the main storm belts at high latitudes. Our results indicate that most of the P-wave sources are within these belts, implying that the interference of waves far from storm activity does not significantly contribute to the microseismic body wave spectrum. Comparison of our results (Figure 12a,b) to the model of Arduin et al. [2011] finds a striking amount of agreement (e.g., see their Figure 7b) as we have found microseismic P-wave detection clusters for all of their seismic sources in the North Atlantic, South Atlantic and Indian ocean. Our results only indicate one additional source missing from their model: the WR-RGR. This minor discrepancy may be the result of a bias in bathymetric excitation coefficients [Tanimoto, 2007] as Ardhuin et al. [2011; 2012] use those of Longuet-Higgins [1950].

4.5 Location Error

Source location error from frequency-slowness analysis is manifested from low f-s spectrum resolution and can make two or more seismic sources appear as a single source located near the center of the cluster. This does not account though for bias in the location from the velocity structure of the Earth. We have investigated this effect for all peaks picked in the P-wave slowness range. The discrepancy between the uncorrected and corrected locations is typically less than 2º, but may be as much as 4º (Figure 12a). This affects the interpretation of P-wave microseism sources near the coast and should be performed for spectra that have resolution lengths smaller than this effect. The effect on our SPDF P-wave source locations is given by Figure 12b where the corrected locations are given by stars and the correction vectors extend to the uncorrected location. One interesting aspect we found is that the source locations to the Southwest of Conrad Rise move closer to that feature. This may be the effect of the large, low-shear velocity province in the lower mantle below Africa and indicates that this source region can provide new constraint on that mantle structure. Repeating the correction procedure for velocity structure bias on the corrected locations gives similar slowness bias to the original locations (Figure 12c) and confirms the assumption that the bias varies little over the scale lengths of the corrections is valid and that the corrected locations are sufficient to account for the assumed velocity structure.

5. Conclusions

Using frequency-slowness analysis of multiple broadband seismometer arrays, we presented evidence that monthly averages of body wave microseisms propagating through equatorial and southern Africa are consistent with locations that microseism theory indicates are optimal for their generation from wave-wave interference [Longuet-Higgins, 1950; Kedar et al.,

2008; Ardhuin et al., 2011]. Looking at the frequency dependence in our data we found that our sources of LPDF (7.5-10s) and SPDF (5-7.5s) microseisms had substantial differences that implied the bathymetry below the interference region plays a critical role in the excitation of body wave microseisms, corroborating previous theory [Longuet-Higgins, 1950; Tanimoto, 2007]. Utilizing these variations with frequency will provide a better source distribution for tomography studies incorporating body wave microseisms. Our northern and southern hemisphere body wave sources also have seasonality consistent with extratropical cyclone activity. The study of body wave microseisms may be useful for monitoring the relative strength of the two storm belts independently from satellite-based studies [e.g., Guo et al., 2009]. Corrections to our source locations for bias from seismic velocity structure shows a potentially significant impact on our interpretation of some sources. We suggest that studies requiring high-resolution P-wave microseism source locations (e.g., for tomography) should account for this bias by simultaneous inversion for source location and structure. The observed behavior of P-wave microseisms from the APC, CR, and WR-RGR were found to be inconsistent with expectations based on bathymetric excitation. These may be related to recent discrepancies noted in the bathymetric excitation coefficients [Tanimoto, 2007] and warrant further investigation.

Acknowledgements

We would like to thank the IRIS DMC, PASSCAL and the numerous field crews for collecting and making available the seismic data from the 4 arrays in this study. This work was supported by NSF EAR-XXXXXX.

References

Ardhuin, F., Stutzmann, E., Schimmel, M., Mangeney, A., 2011, Ocean wave sources of seismic noise, *J. Geophys. Res.*, Vol. 116, C09004, doi:10.1029/2011JC006952

Ardhuin, F., Balanche, A., Stutzmann, E., Obrebski, M., 2012, From seismic noise to ocean wave parameters: General methods and validation, *J. Geophys. Res.*, Vol. 117, C05002, doi:10.1029/2011JC007449

Aster, R. C., McNamara, D. E., Bromirski, P. D., 2008, Multidecadal climate-induced variability in microseisms, *Seismol. Res. Lett.*, Vol. 79, No. 2, pp. 194-202, doi:10.1785/gssrl.79.2.194

Aster, R. C., McNamara, D. E., Bromirski, P. D., 2010, Global trends in extremal microseism intensity, *Geophys. Res. Lett.*, Vol. 37, L14303, doi:10.1029/2010GL043472

Astiz, L., Earle, P. S., Shearer, P. M., 1996, Global stacking of broadband seismograms, *Seismol. Res. Lett.*, Vol. 67, No. 4, pp. 8-18

Backus, M., Burg, J., Baldwin, D., Bryan, E., 1964, Wide-band extraction of mantle P waves from ambient noise, *Geophysics*, Vol. 29, No. 5, pp. 672-692, doi:10.1190/1.1439404

Bassin, C., Laske, G., Masters, G., 2000, The Current Limits of Resolution for Surface Wave Tomography in North America, *EOS Trans. Am. Geophys. Un.*, 81 (48), Fall Meet. Suppl., Abstract S12A-03

Bastow, I. D., Nyblade, A. A., Stuart, G. W., Rooney, T. O., Benoit, M. H., 2008, Upper mantle

seismic structure beneath the Ethiopian hot spot: Rifting at the edge of the African low-velocity anomaly, *Geochem. Geophys. Geosyst.*, Vol. 9, No. 12, Q12022, doi:10.1029/2008GC002107

Benson, G.D., Ritzwooller, M.H., Barmin, M.P., Levshin, A.L., Lin, F., Moschetti, M.P., Shapiro, N.M., Yang, Y., 2007, Processing seismic ambient noise data to obtain reliable broad-band surface wave dispersion measurements, *Geophys. J. Int.*, Vol. 169, pp. 1239-1260, doi:10.1111/j.1365-246X.2007.03374.x

Brenguier, F., Campillo, M., Hadziioannou, C., Shapiro, N. M., Nadeau, R. M., Larose, E., 2008a, Postseismic relaxation along the San Andreas fault at Parkfield from continuous seismological observations, *Science*, Vol. 321, pp. 1478-1481, doi:10.1126/science.1160943

Brenguier, F., Shapiro, N. M., Campillo, M., Ferrazzini, V., Duputel, Z., Coutant, O., Nercessian, A., 2008b, Towards forecasting volcanic eruptions using seismic noise, *Nature Geoscience*, Vol. 1, No. 2, pp. 126-130, doi:10.1038/ngeo104

Bromirski, P. D., Duennebier, F. K., 2002, The near-coastal microseism spectrum: spatial and temporal wave climate relationships, *J. Geophys. Res.*, Vol. 107, No. B8, doi:10.1029/2001JB000265

Bromirski, P. D., Duennebier, F. K., Stephen, R. A., 2005, Mid-ocean microseisms, *Geochem. Geophys. Geosyst.*, Vol. 6, No. 4, Q04009, doi:10.1029/2004GC000768

Burg, J. P., 1964, Three-dimensional filtering with an array of seismometers, *Geophysics*, Vol.

29, No. 5, pp. 693-713, doi:10.1190/1.1439406

Capon, J., 1969, High-resolution frequency-wavenumber spectrum analysis, *Proc. IEEE*, Vol. 57, No. 8, pp. 1408-1418, doi:10.1109/PROC.1969.7278

Capon, J., 1973, Analysis of microseismic noise at LASA, NORSAR, and ALPA, *Geophys. J. R. astr. Soc.*, Vol. 35, pp. 39-54, doi:10.1111/j.1365-246X.1973.tb02413.x

Cessaro, R. K., 1994, Sources of primary and secondary microseisms, *Bull. Seismol. Soc. Am.*, Vol. 84, No. 1, pp. 142-148

Cessaro, R. K., Chan, W. W., 1989, Wide-angle triangulation array study of simultaneous primary microseism sources, *J. Geophys. Res.*, Vol. 94, No. B11, pp. 15,555–15,563, doi:10.1029/JB094iB11p15555

Chevrot, S., Sylvander, M., Benahmed, S., Ponsolles, C., Lefevre, J. M., Paradis, D., 2007, Source locations of secondary microseisms in western Europe: evidence for both coastal and pelagic sources, *J. Geophys. Res.*, Vol. 112, B11301, doi:10.1029/2007JB005059

Darbyshire, J., 1963, A study of microseisms in South Africa, *Geophys. J. R. astr. Soc.*, Vol. 8, pp. 165-175, doi:10.1111/j.1365-246X.1963.tb06280.x

Dugda, M. T., Nyblade, A. A., Julià, J., Langston, C. A., Ammon, C. J., Simiyu, S., 2005, Crustal structure in Ethiopia and Kenya from receiver function analysis: Implications for rift

development in eastern Africa, *J. Geophys. Res.*, Vol. 110, B01303, doi:10.1029/2004JB003065

Fouch, M. J., James, D. E., VanDecar, J. C., van der Lee, S., Kaapvaal Seismic Group, 2004, Mantle seismic structure beneath the Kaapvaal and Zimbabwe Cratons, *S. Afric. J. Geol.*, Vol. 107, pp. 33-44, doi:10.2113/107.1-2.33

Friedrich, A., Kruger, F., Klinge, K., 1998, Ocean-generated microseismic noise located with the Grafenberg array, *J. of Seis.*, Vol. 2, pp. 47-64, doi:10.1023/A:1009788904007

Gerstoft, P., Fehler, M. C. Sabra, K. G., 2006, When Katrina hit California, *Geophys. Res. Lett.*, Vol. 33, L17308, doi:10.1029/2006GL027270

Gerstoft, P., Shearer, P. M., Harmon, N., Zhang, J., 2008, Global P, PP, and PKP wave microseisms observed from distant storms, *Geophys. Res. Lett.*, Vol. 35, L23306, doi:10.1029/2008GL036111

Gerstoft, P., Tanimoto, T., 2007, A year of microseisms in southern California, *Geophys. Res. Lett.*, Vol. 34, L20304, doi:10.1029/2007GL031091

Grob, M., Maggi, A., Stutzmann, E., 2011, Observations of the seasonality of the Antarctic microseismic signal, and its association to sea ice variability, *Geophys. Res. Lett.*, Vol. 38, L11302, doi:10.1029/2011GL047525

Guo, Y., Chang, E. K. M., Leroy, S. S., 2009, How strong are the southern hemisphere storm

tracks?, *Geophys. Res. Lett.*, Vol. 36, L22806, doi:10.1029/2009GL040733

Harmon, N., Rychert, C., Gerstoft, P., 2010, Distribution of noise sources for seismic interferometry. *Geophys. J. Int.*, Vol. 183, pp. 1470–1484, doi:10.1111/j.1365-246X.2010.04802.x

Hasselmann, K., 1963, A statistical analysis of the generation of microseisms, *Rev. Geophys.*, Vol. 1, No. 2, pp. 177-210, doi:10.1029/RG001i002p00177

Haubrich, F. A., 1968, Array Design, *Bull. Seismol. Soc. Am.*, Vol. 58, No. 3, pp. 977-991

Haubrich, F. A., McCamy, K., 1969, Microseisms: coastal and pelagic sources, *Rev. Geophys.*, Vol. 7, No. 3, pp. 539-571, doi:10.1029/RG007i003p00539

Haubrich, R.A., Munk, W.H., Snodgrass, F.E., 1963, Comparative spectra of microseisms and swell, *Bull. Seismol. Soc. Am.*, Vol. 53, No. 1, pp. 27-37

Houser, C., Masters, G., Shearer, P., Laske, G., 2008, Shear and compressional velocity models of the mantle from cluster analysis of long-period waveforms, *Geophys. J. Int.*, Vol. 174, No. 1, pp. 195-212, doi:10.1111/j.1365-246X.2008.03763.x

James, D. E., Fouch, M. J., VanDecar, J. C., van der Lee, S., Kaapval Seismic Group, 2001, Tectospheric structure beneath southern Africa, *Geophys. Res. Lett.*, Vol. 28, No. 13, pp. 2485-2488, doi:10.1029/2000GL012578

James, D. E., Niu, F., Rokosky, J., 2003, Crustal structure of the Kaapvaal craton and its significance for early crustal evolution, *Lithos*, Vol. 71, pp. 413-429, doi:10.1016/j.lithos.2003.07.009

Julià, J., Ammon, C. J., Nyblade, A. A., 2005, Evidence for mafic lower crust in Tanzania, East Africa, from joint inversion of receiver functions and Rayleigh wave dispersion velocities, *Geophys. J. Int.*, Vol. 162, pp. 555-569, doi:10.1111/j.1365-246X.2005.02685.x

Kedar, S., Longuet-Higgens, M., Webb, F., Graham, N., Clayton, R., Jones, C., 2008, The origin of deep ocean microseisms in the North Atlantic Ocean, *Proc. R. Soc. A*, Vol. 464, pp. 777-793, doi:10.1098/rspa.2007.0277

Kennett, B. L. N., Engdahl, E. R., Buland, R., 1995, Constraints on seismic velocities in the Earth from travel times, *Geophys. J. Int.*, Vol. 122, pp. 108-124, doi:10.1111/j.1365-246X.1995.tb03540.x

Kennett, B. L. N., Gudmundsson, O., 1996, Ellipticity corrections for seismic phases, *Geophys. J. Int.*, Vol. 127, pp. 40-48, doi:10.1111/j.1365-246X.1996.tb01533.x

Kim, S., Nyblade, A. A., Rhie, J., Baag, C.-E., Kang, T.-S., 2012, Crustal S-wave velocity structure of the Main Ethiopian Rift from ambient noise tomography, *Geophys. J. Int.*, Vol. 191, pp. 865-878, doi:10.1111/j.1365-246X.2012.05664.x

Koch, F. W., Wiens, D. A., Nyblade, A. A., Shore, P. J., Tibi, R., Ateba, B., Tabod, C. T., Nnange, J. M., 2012, Upper-mantle anisotropy beneath the Cameroon volcanic line and Congo craton from shear wave splitting measurements, *Geophys. J. Int.*, Vol. 190, No. 1, pp. 75-86, doi:10.1111/j.1365-246X.2012.05497.x

Koper, K. D., de Foy, B., 2008, Seasonal anisotropy in short-period seismic noise recorded in South Asia, *Bull. Seismol. Soc. Am.*, Vol. 98, No. 6, pp. 3033-3045, doi:10.1785/0120080082

Koper, K. D., de Foy, B., Benz, H., 2009, Composition and variation of noise recorded at the Yellowknife seismic array, 1991-2007, *J. Geophys. Res.*, Vol. 114, B10310, doi:10.1029/2009JB006307

Koper, K. D., Seats, K., Benz, H. M., 2010, On the composition of Earth's short period seismic noise field, *Bull. Seismol. Soc. Am.*, Vol. 100, No. 2, pp. 606-617, doi:10.1785/0120090120

Lacoss, R. T., Kelly, E. J., Toksöz, N. M., 1969, Estimation of seismic noise structure using arrays, *Geophysics*, Vol. 34, No. 1, pp. 21-38, doi:10.1190/1.1439995

Landes, M., Hubans, F., Shapiro, N. M., Paul, A., Campillo, M., 2010, Origin of deep ocean microseisms by using teleseismic body waves, *J. Geophys. Res.*, Vol. 115, B05302, doi:10.1029/2009JB006918

Lawrence, J. F., Prieto, G. A., 2011, Attenuation tomography in the western United States from ambient seismic noise. *J. Geophys. Res.*, Vol. 116, B06302, doi:10.1029/2010JB007836

Lin, F.-C., Moschetti, M. P., Ritzwoller, M. H., 2008, Surface wave tomography of the western United States from ambient seismic noise: Rayleigh and Love wave phase velocity maps, *Geophys. J. Int.*, Vol. 173, pp. 281-298, doi:10.1111/j.1365-246X.2008.03720.x

Lin, F.-C. Ritzwoller, M. H., 2011, Helmholtz surface wave tomography for isotropic and azimuthally anisotropic structure, *Geophys. J. Int.* , Vol. 186, pp. 1104–1120, doi:10.1111/j.1365-246X.2011.05070.x

Lin, F.-C., Ritzwoller, M. H., Snieder, R., 2009, Eikonal tomography: surface wave tomography by phase front tracking across a regional broad-band seismic array, *Geophys. J. Int.*, Vol. 177, pp. 1091–1110, doi:10.1111/j.1365-246X.2009.04105.x

Lin, F.-C., Schmandt, B., Tsai, V. C., 2012, Joint inversion of Rayleigh wave phase velocity and ellipticity using USArray: constraining velocity and density structure in the upper crust, *Geophys. Res. Lett.*, Vol. 39, L12303, doi:10.1029/2012GL052196

Lin, F.-C., Tsai, V. C., Ritzwoller, M. H., 2012, The local amplification of surface waves: a new observable to constrain elastic velocities, density, and anelastic attenuation, *J. Geophys. Res.*, Vol. 117, B06302, doi:10.1029/2012JB009208

Longuet-Higgens, M. S., 1950, A theory of the origin of microseisms, *Phil. Trans. R. Soc. Lond. A*, Vol. 243, No. 857, pp. 1-35, doi:10.1098/rsta.1950.0012

McNamara, D. E., Buland, R. P., 2004, Ambient noise levels in the continental United States, *Bull. Seismol. Soc. Am.*, Vol. 94, No. 4, pp. 1517-1527, doi:10.1785/012003001

Nolet, G., 2008, *A breviary of seismic tomography: imaging the interior of the earth and sun*, Cambridge University Press, New York

Nyblade, A. A., Birt, C., Langston, C. A., Owens, T. J., Last, R. J., 1996, Seismic experiment reveals rifting of craton in Tanzania, *Eos Trans. AGU*, Vol. 77, No. 51, pp. 517-519, doi:10.1029/96EO00339

Nyblade, A. A., Langston, C. A., 2002, Broadband seismic experiments probe the East African Rift, *Eos Trans. AGU*, Vol. 83, No. 37, pp. 405, doi:10.1029/2002EO000296

Obrebski, M. J., Arduin, F., Stutzmann, E., Schimmel, M., 2012, How moderate sea states can generate loud seismic noise in the deep ocean, *Geophys. Res. Lett.*, Vol. 39, L11601, doi:10.1029/2012GL051896

Peterson, J., 1993, Observation and modeling of seismic background noise, *U.S. Geol. Surv. Tech. Rept. 93-322*, I-95

Prieto, G. A., Lawrence, J. F., Beroza, G. C., 2009, Anelastic Earth structure from the coherency of the ambient seismic field, *J. Geophys. Res.*, 114, B07303, doi:10.1029/2008JB006067

Ramirez, J. E., 1940, An experimental investigation of the nature and origin of microseisms at

St. Louis, Missouri: Part one, *Bull. Seismol. Soc. Am.*, Vol. 30, No. 1, pp. 35-84

Ramirez, J. E., 1940, An experimental investigation of the nature and origin of microseisms at St. Louis, Missouri: Part two, *Bull. Seismol. Soc. Am.*, Vol. 30, No. 2, pp. 139-178

Reusch, A. M., Nyblade, A. A., Tibi, R., Wiens, D. A., Shore, P. J., Bekoa, A., Tabod, C. T., Nnange, J. M., 2011, Mantle transition zone thickness beneath Cameroon: evidence for an upper mantle origin for the Cameroon volcanic line, *Geophys. J. Int.*, Vol. 187, pp. 1146–1150, doi:10.1111/j.1365-246X.2011.05239.x

Reusch, A. M., Nyblade, A. A., Wiens, D. A., Shore, P. J., Ateba, B., Tabod, C. T., Nnange, J. M., 2010, Upper mantle structure beneath Cameroon from body wave tomography and the origin of the Cameroon volcanic line, *Geochem. Geophys. Geosyst.*, Vol. 11, Q10W07, doi:10.1029/2010GC003200

Rost, S., Thomas, C., 2002, Array seismology: methods and applications, *Rev. Geophys.*, Vol. 40, No. 3, pp. 1008-1034, doi:10.1029/2000RG000100

Rost, S., Thomas, C., 2009, Improving seismic resolution through array processing techniques, *Surv. Geophys.*, Vol. 30, pp. 271-299, doi:10.1007/s10712-009-9070-6

Sabra, K. G., Gerstoft, P., Roux, P., Kuperman, W. A., Fehler, M. C., 2005, Extracting time-domain Green's function estimates from ambient seismic noise, *Geophys. Res. Lett.* , Vol. 32, L03310, doi:10.1029/2004GL021862

Schulte-Pelkum, V., Earle, P. S., Vernon, F. L., 2004, Strong directivity of ocean-generated seismic noise, *Geochem. Geophys. Geosyst.*, Vol. 5, No. 3, Q03004, doi:10.1029/2003GC000520

Seats, K. J., Lawrence, J. F., Prieto, G. A., 2012, Improved ambient noise correlation functions using Welch's method. *Geophys. J. Int.*, Vol. 188, pp. 513–523, doi:10.1111/ j.1365-246X.2011.05263.x

Sens-Schönfelder, C., Wegler, U., 2006, Passive image interferometry and seasonal variations of seismic velocities at Merapi Volcano, Indonesia, *Geophys. Res. Lett.*, Vol. 33, L21302, doi:10.1029/2006GL027797

Shapiro, N. M., Ritzwoller, M. H., Bensen, G. D., Source location of the 26 sec microseism from cross-correlations of ambient seismic noise, *Geophys. Res. Lett.*, Vol. 33, L18310, doi:10.1029/2006GL027010

Sheen, D.-H., Shin, J. S., Kang, T.-S., Baag, C.-E., 2009, Low frequency cultural noise, *Geophys. Res. Lett.*, Vol. 36, L17314, doi:10.1029/2009GL039625

Stehly, L., Campillo, M., Shapiro, N. M., 2006, A study of the seismic noise from its long-range correlation properties, *J. Geophys. Res.*, Vol. 111, B10306, doi:10.1029/2005JB004237

Stutzmann, E., Schimmel, M., Patau, G., Maggi, A., 2009, Global climate imprint on seismic noise, *Geochem. Geophys. Geosyst.*, Vol. 10, No. 11, Q11004, doi:10.1029/2009GC002619

Tanimoto, T., 2007, Excitation of microseisms, *Geophys. Res. Lett.*, Vol. 34, L05308, doi:10.1029/2006GL029046

Tokam, A. K., Tabod, C. T., Nyblade, A. A., Julià, J., Wiens, D. A., Pasyanos, M. E., 2010, Structure of the crust beneath Cameroon, West Africa, from the join inversion of Rayleigh wave group velocities and receiver functions, *Geophys. J. Int.*, Vol. 183, No. 2, pp. 1061-1076, doi:10.1111/j.1365-246X.2010.04776.x

Toksöz, M. N., Lacoss, R. T., 1968, Microseisms: mode structure and sources, Science, Vol. 159, No. 3817, pp. 872-873, doi:10.2307/1724279

Tolman, H. L., 2009, User manual and system documentation of WAVEWATCH III version 3.14, NOAA / NWS / NCP / MMAB Technical Note 276

Tsai, V. C., 2009, On establishing the accuracy of noise tomography travel-time measurements in a realistic medium, *Geophys. J. Int.*, Vol. 178, pp. 1555-1564, doi:10.1111/j.1365-246X.2009.04239.x

Webb, S. C., 1992, The equilibrium oceanic microseism spectrum, *J. Acoust. Soc. Am.*, Vol. 92, No. 4-1, pp. 2141-2158, doi:10.1121/1.405226

Webb, S. C., 2008, The Earth's hum: the excitation of Earth normal modes by ocean waves, *Geophys. J. Int.*, Vol. 174, pp. 542-566, doi:10.1111/j.1365-246X.2008.03801.x

Weeraratne, D. S., Forsyth, D. W., Fischer, K. M., Nyblade, A. A., 2003, Evidence for an upper mantle plume beneath the Tanzanian craton from Rayleigh wave tomography, *J. Geophys. Res.*, Vol. 108, B92427, doi:10.1029/2002JB002273

Wegler, U., Sens-Schönfelder, C., 2007, Fault zone monitoring with passive image interferometry, *Geophys. J. Int.*, Vol. 168, pp. 1029-1033, doi:10.1111/j.1365-246X.2006.03284.x

Welch, P. D., 1967, The use of fast Fourier transform for the estimation of power spectra: a method based on time averaging over short, modified periodograms, *IEEE Trans. Audio and Electroacoust.*, Vol. AU-15, pp. 70-73, doi:10.1109/TAU.1967.1161901

Westwood, E. K., 1992, Broadband matched-field source localization, *J. Acoust. Soc. Am.*, Vol. 91, No. 5, pp. 2777-2789, doi:10.1121/1.402958

Yang, Y., Li, A., Ritzwoller, M.H., 2008, Crustal and uppermost mantle structure in southern Africa from ambient noise and teleseismic tomography, *Geophys. J. Int.*, doi:10.1111/j.1365-246X.2008.03779.x

Yang, Y., Ritzwoller, M. H., 2008, Characteristics of ambient seismic noise as a source for surface wave tomography, *Geochem. Geophys. Geosyst.*, Vol. 9, No. 2, doi:10.1029/2007GC001814

Zhang, J., Gerstoft, P., Bromirski, P.D., 2010a, Pelagic and coastal sources of P-wave microseisms: Generation under tropical cyclones, *Geophys. Res. Lett.*, Vol. 37, L15301, doi:10.1029/2010GL044288

Zhang, J., Gerstoft, P., Shearer, P.M., 2009, High-frequency P-wave seismic noise driven by ocean winds, *Geophys. Res. Lett.*, Vol. 36, L09302, doi:10.1029/2009GL037761

Zhang, J., Gerstoft, P., Shearer, P. M., 2010b, Resolving P-wave travel-time anomalies using seismic array observations of oceanic storms, *Earth Planet. Sci. Lett.*, Vol. 292, pp. 419-427, doi:10.1016/j.epsl.2010.02.014

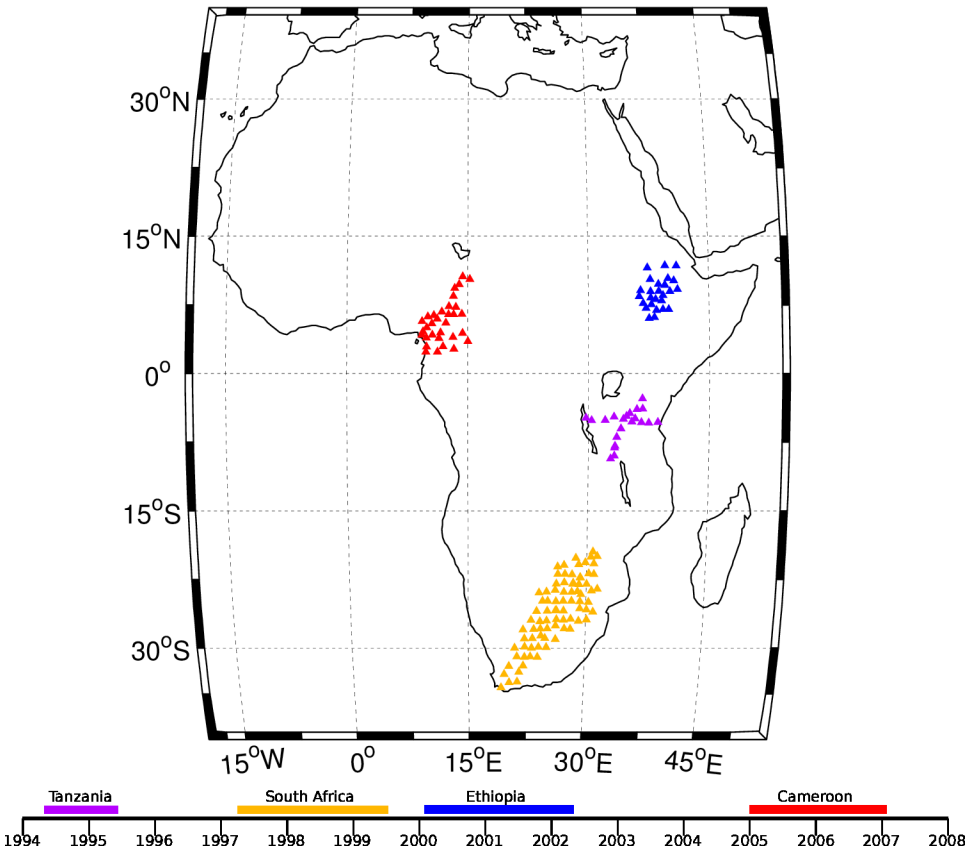

Figure 1. Location and deployment times of the broadband seismometer arrays in this study. There are 4 arrays consisting of the 32 station Cameroon array (red triangles, deployed from January 2005 to January 2007), the 28 station Ethiopia array (blue triangles, deployed from February 2000 to May 2002), the 21 station Tanzania array (purple triangles, deployed from May 1994 to June 1995), and the 82 station South Africa array (yellow triangles, deployed from April 1997 to July 1999).

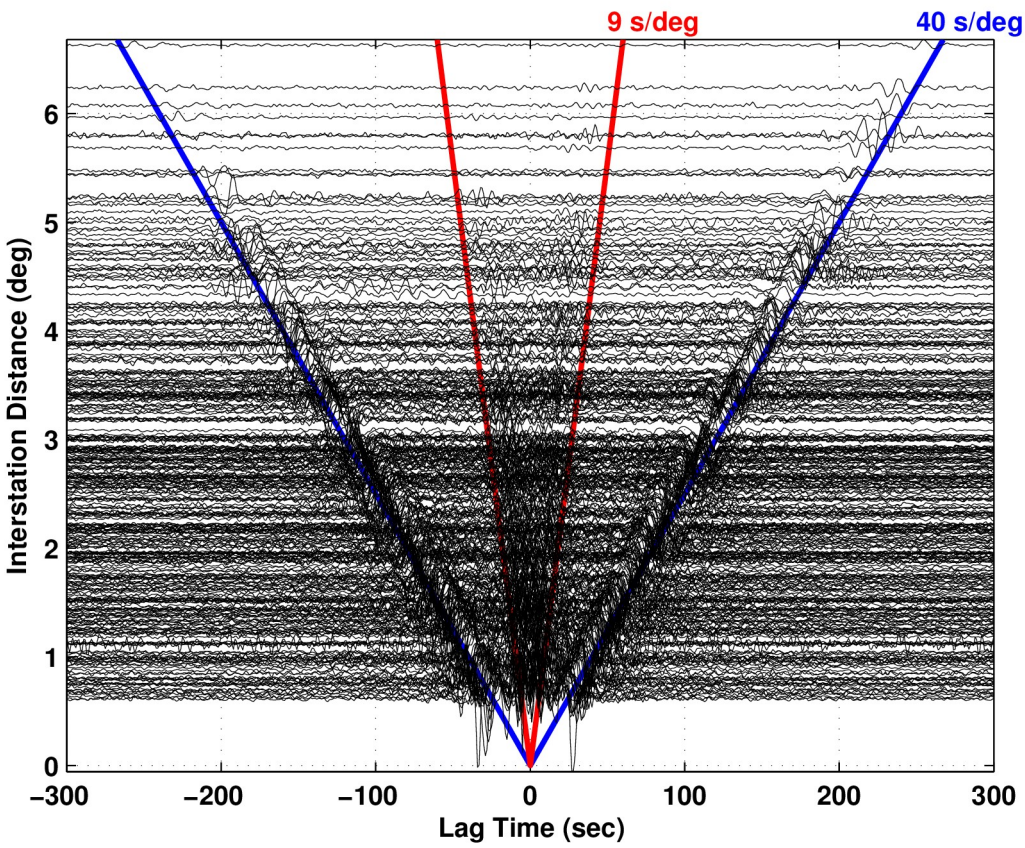

Figure 2. Plot of noise correlations from station pairs in the Ethiopia array as a function of station pair separation. The noise correlations are 2-year stacks (the entire deployment time of the array). Arrivals in positive (causal) time correspond to correlated noise propagating through the source station before the receiver station, while negative (acausal) time indicates the noise arrives at the receiver station first. The arrivals with a slower group velocity of 40s/º are the Rayleigh waves of the partially recovered two-way Green's function of the Earth between each station pair. The arrivals with moveouts higher than 9s/º represent teleseismic body waves consistently arriving from specific abyssal locations and are not part of the interstation Green's function.

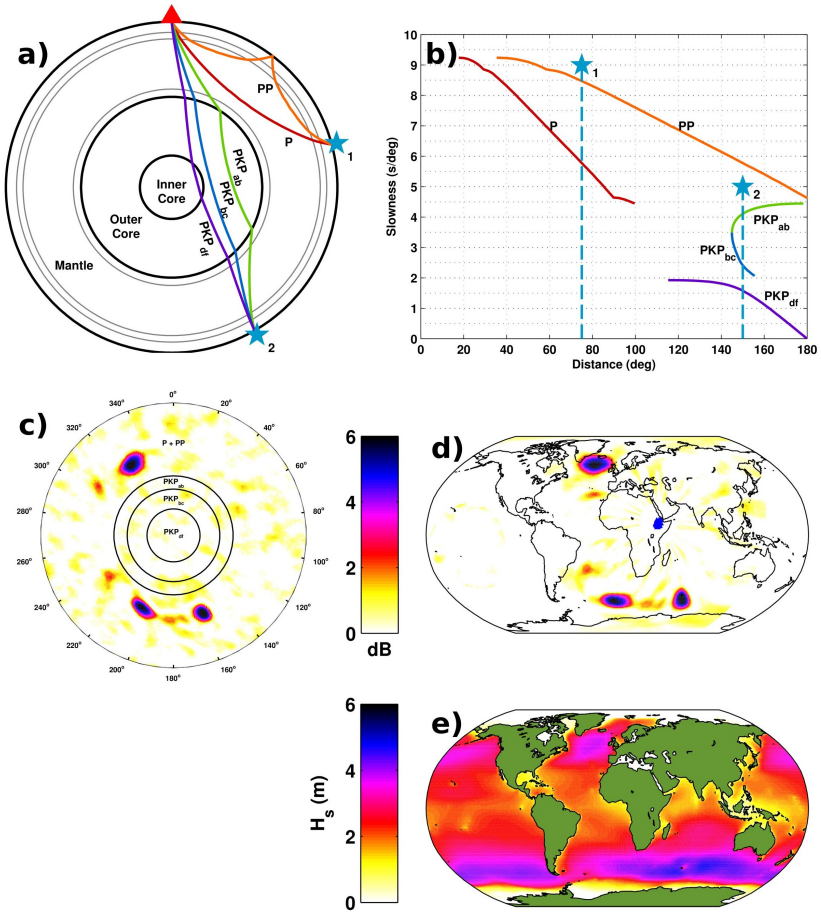

Figure 3. The backprojection of body wave noise from the Ethiopia Array to apparent P-wave source locations. (a) Ray paths of seismic phases expected to have the highest amplitudes [Astiz et al., 1996; Gerstoft et al., 2008]. (b) Plot of the slowness versus distance of those seismic phases from a surface source propagating through the 1D Earth model AK135 [Kennett et al., 1995]. The P & PP slowness curves above 9.25s/° are removed due to triplications. (c) Slowness spectrum for the noise correlations in Figure 2 averaged across the 5-7.5s period band. The spectrum is divided by concentric black rings at 2.0s/°, 3.5s/°, and 4.5s/° corresponding to the different seismic phases shown above. The spectrum is normalized to give 0dB at the median value. (d) P & PKP_{bc} backprojection of the slowness spectrum. (e) Significant wave height hindcasts averaged from February 2000 to May 2002 (the deployment duration).

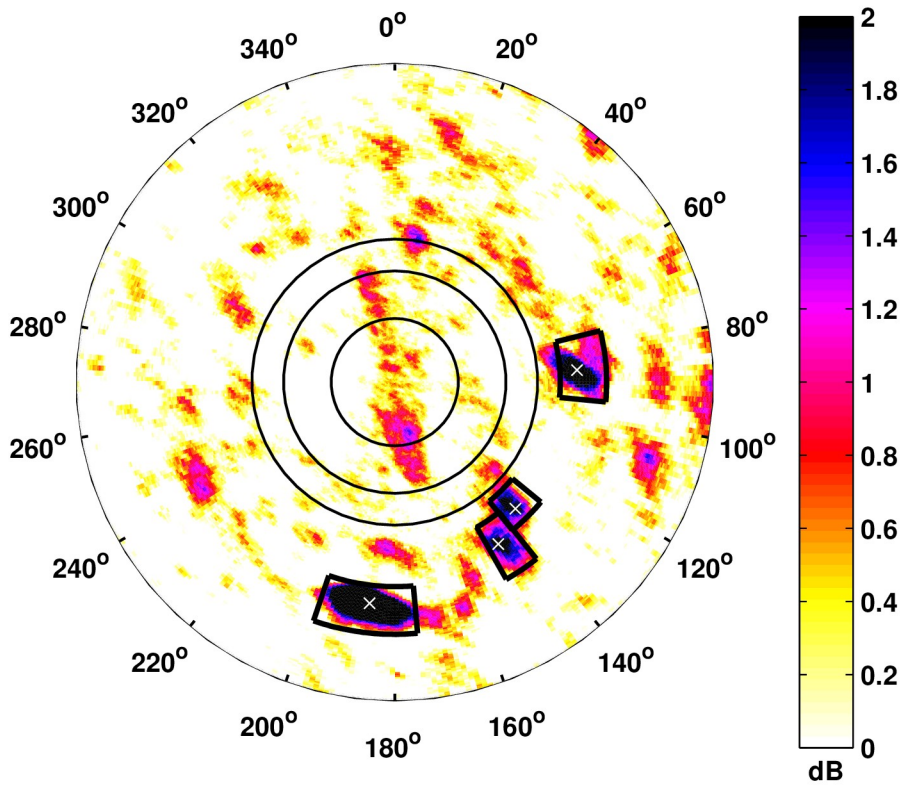

Figure 4. Peaks picked for the Cameroon array June f-s spectrum averaged over 7.5-10s periods. An analyst picks a peak (white X's) by selecting the local slowness-azimuth space (black boxes). Concentric black rings denote seismic phase slowness ranges from Figure 3c. The spectrum is normalized to give 0dB at the median value.

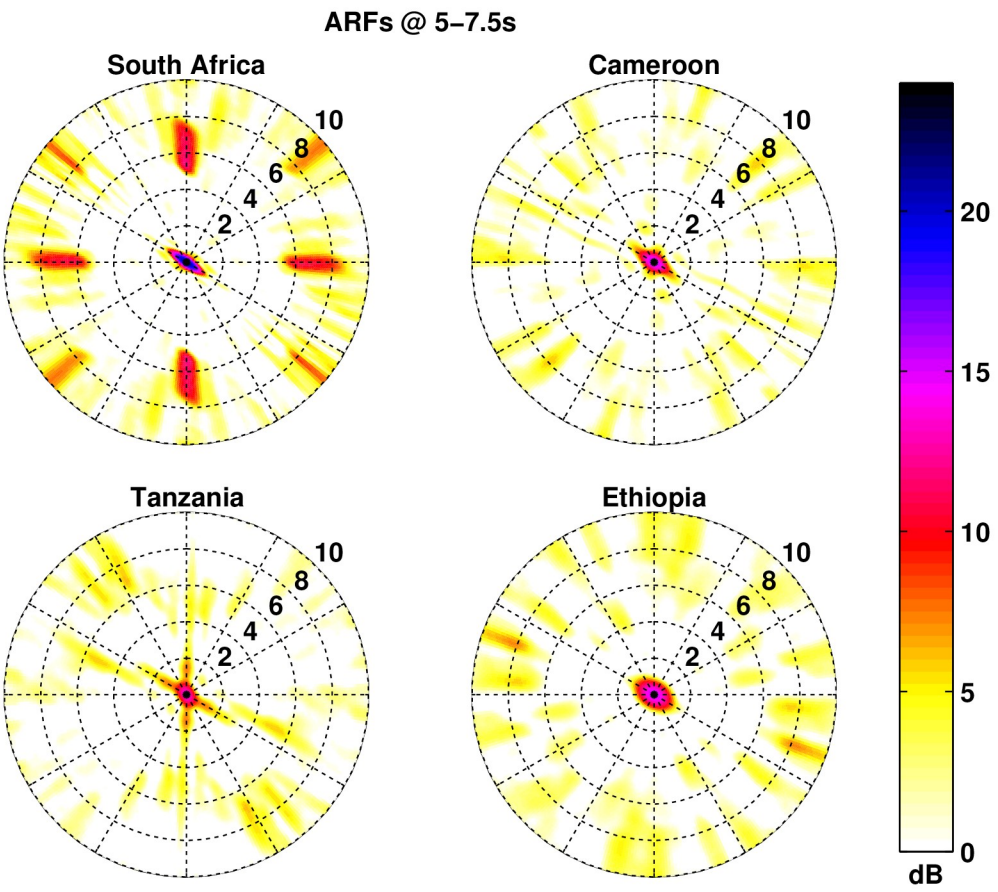

Figure 5a. Array response function (ARF) for each array averaged over the period band 5-7.5s. Each response is normalized to give 0dB at the median value.

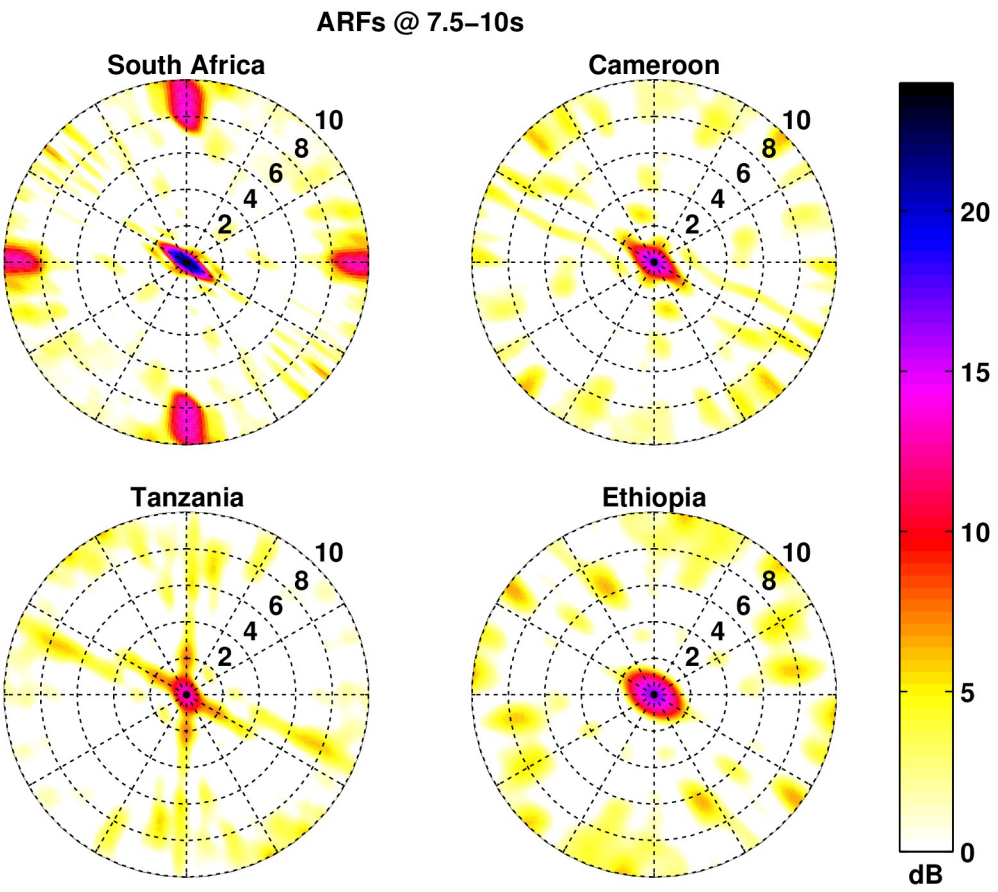

Figure 5b. Same as in Figure 5a except for period band 7.5-10s.

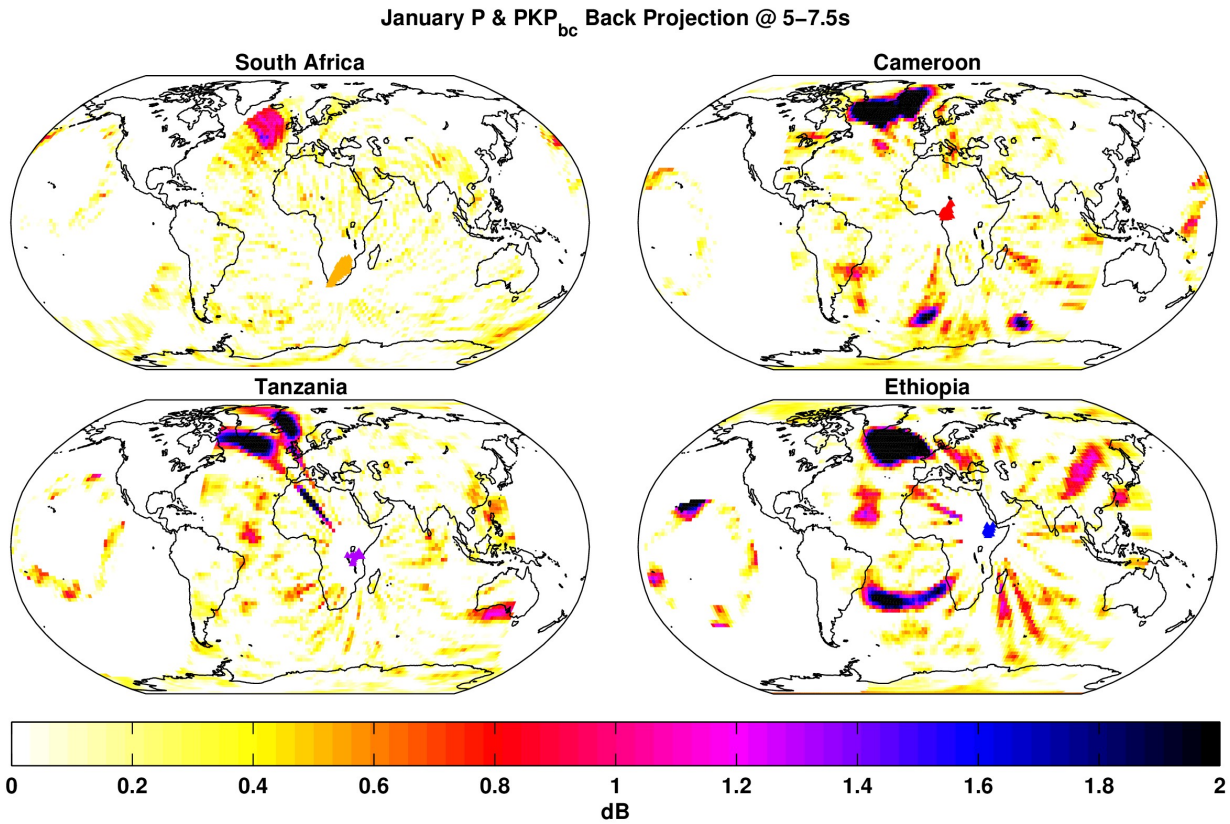

Figure 6a. P & PKPbc backprojection of slowness spectra for each array in January averaged over the 5-7.5s period band. The spectra are normalized to give 0dB at the median value.

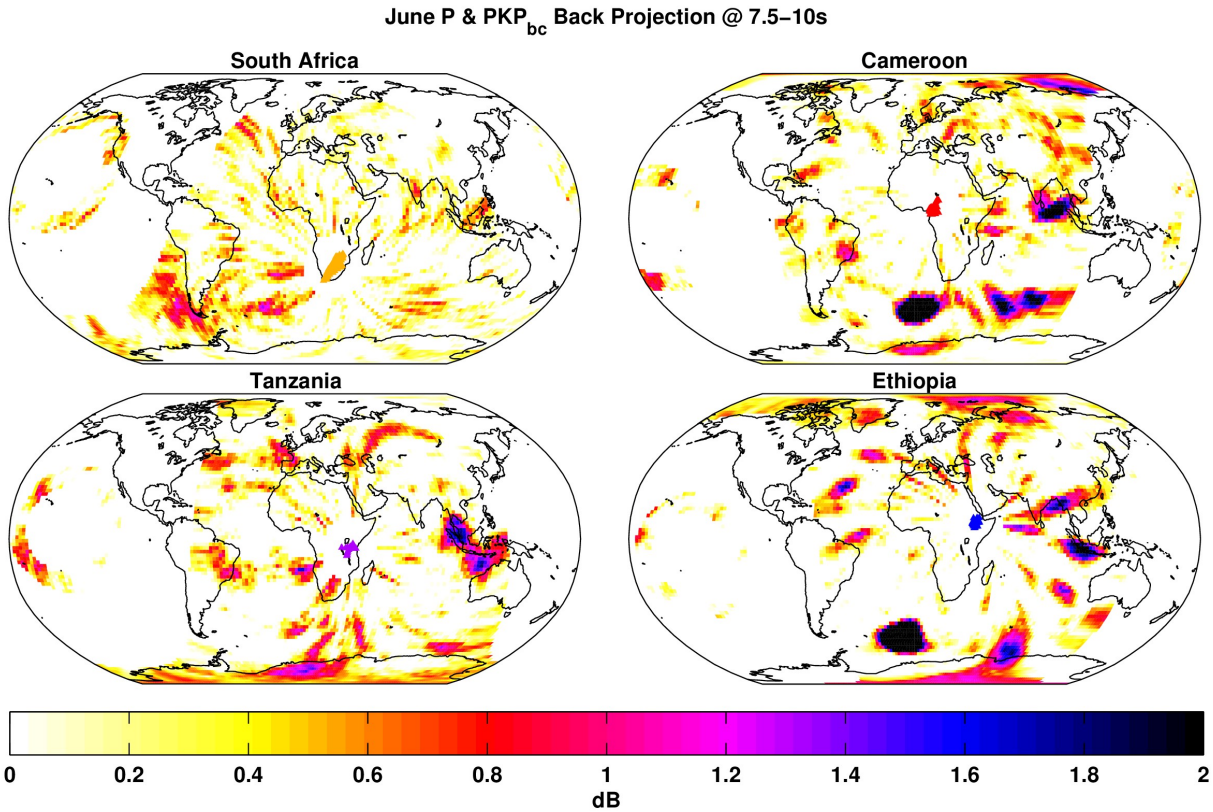

Figure 6b. Same as in Figure 6a except averaged for the month of June for the 7.5-10s period band.

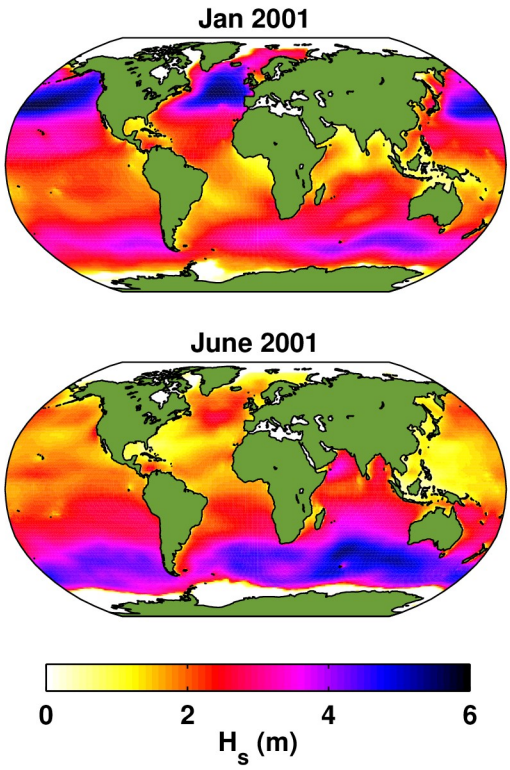

Figure 7. Significant wave heights from the WaveWatch III model [Tolman, 2009] averaged over the months January 2001 and June 2001.

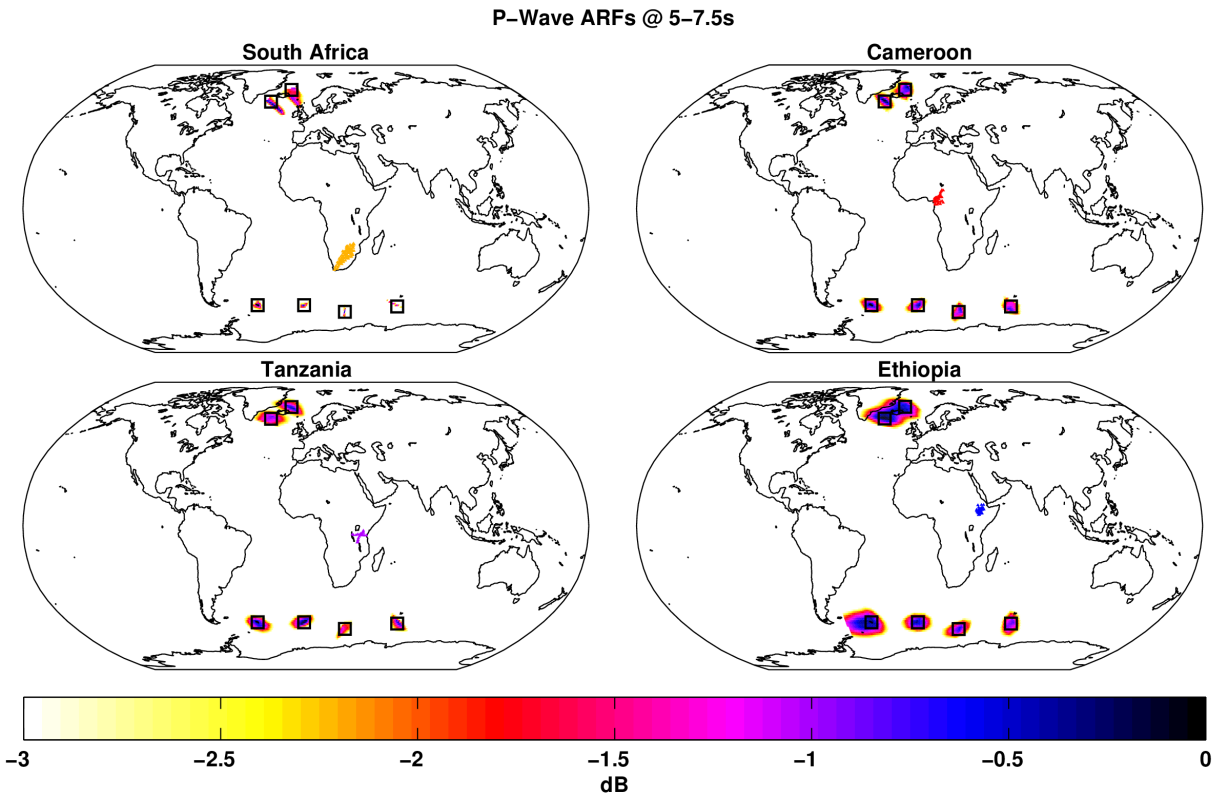

Figure 8a. Backprojection ARFs for multiple source locations (black boxs) of continuous P-waves. Each array has the stations colored as from Figure 1. The responses are averaged over 5-7.5s periods and are normalized to give 0dB at the maximum value.

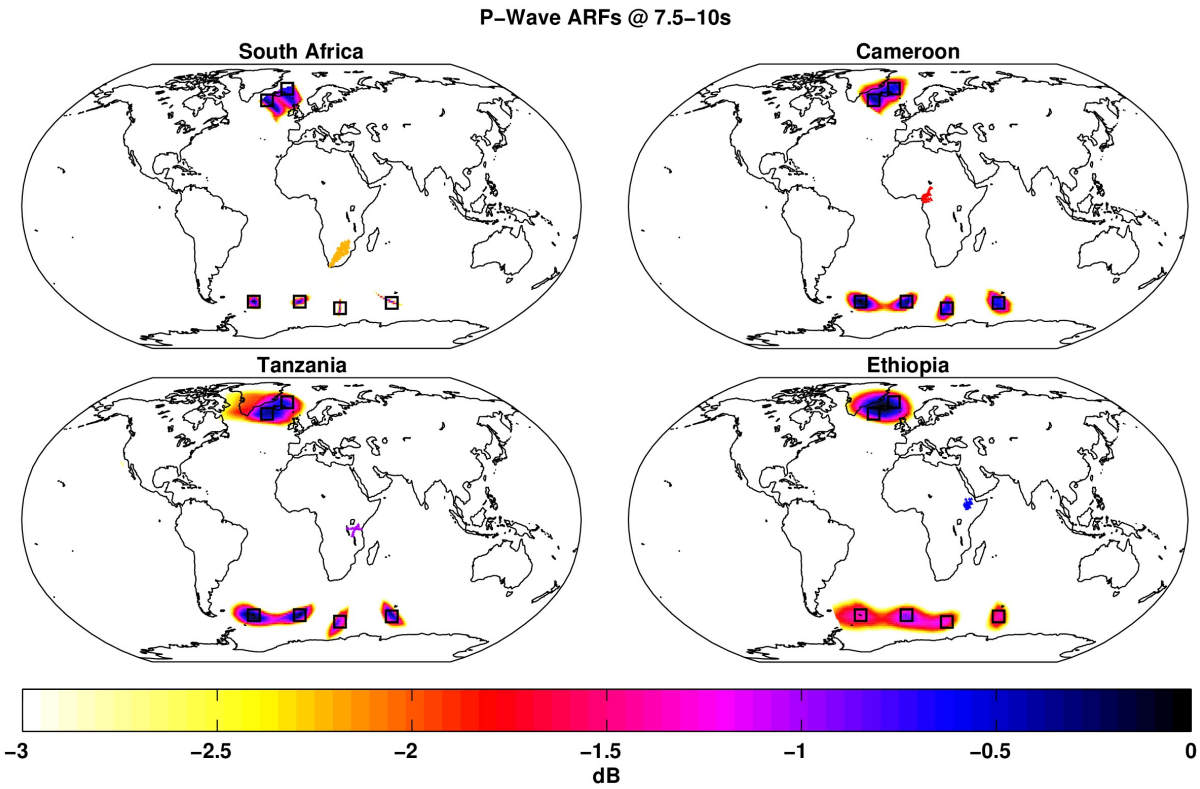

Figure 8b. Same as Figure 8b but for 7.5-10s periods.

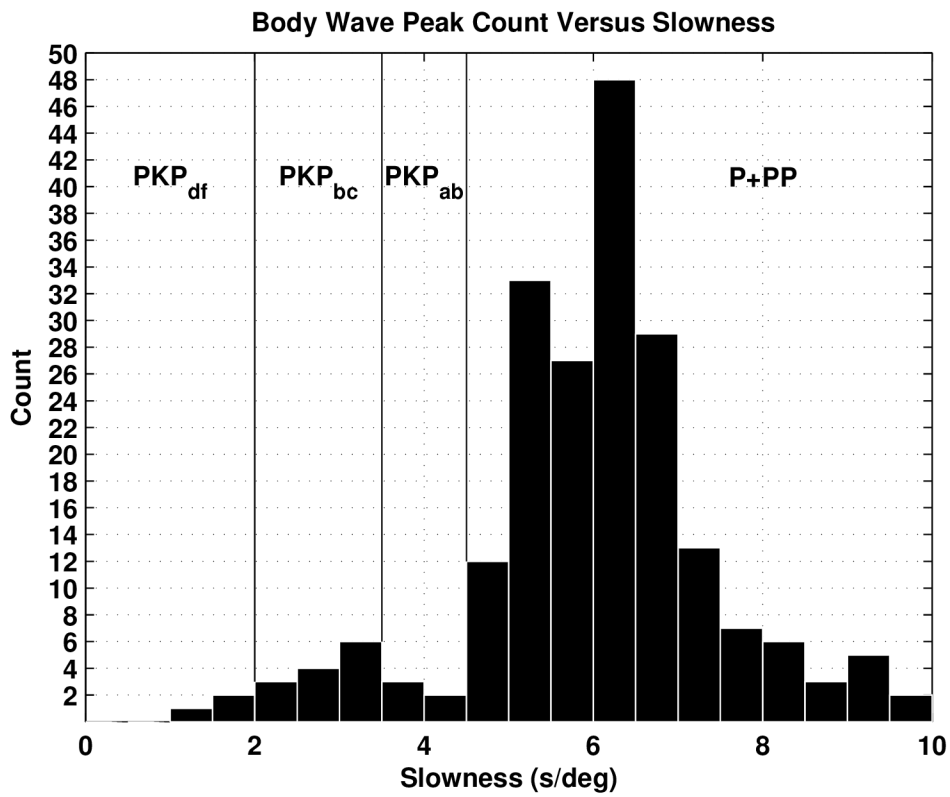

Figure 9a. Number of picked peaks as a function of slowness with 0.5s/º wide bins. Seismic phase slowness ranges are delimited by the solid vertical black lines.

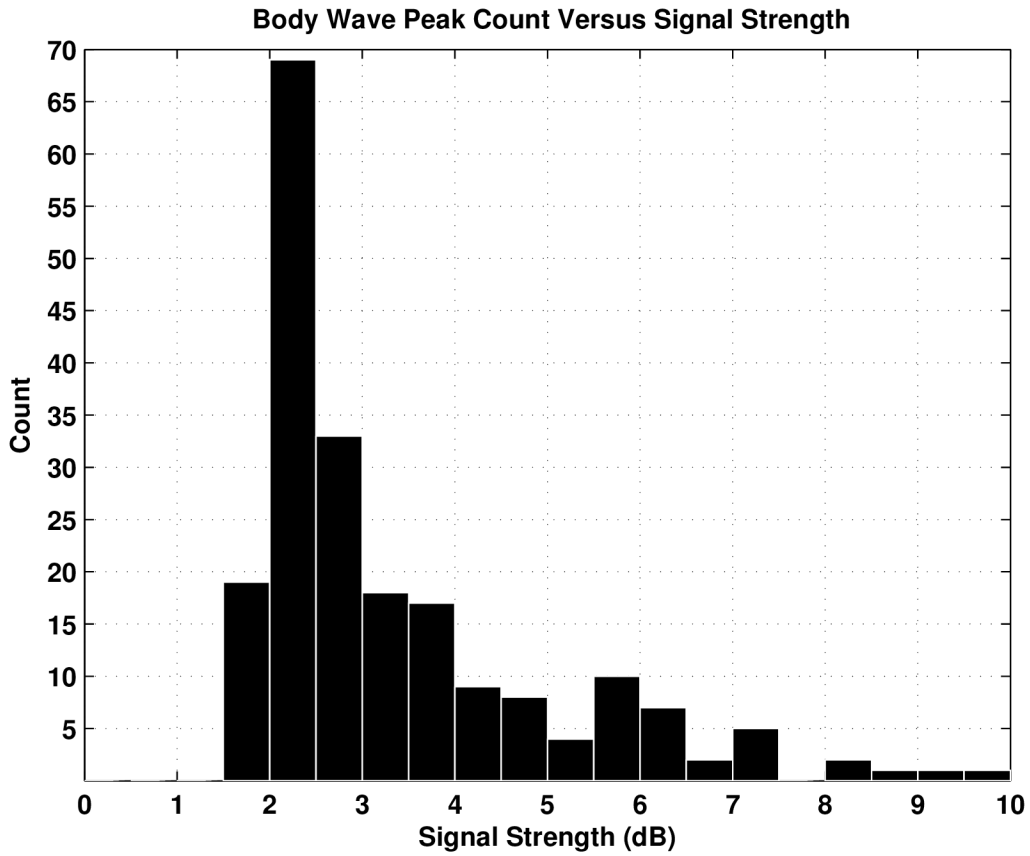

Figure 9b. Histogram of picked peak signal strength in dBs from the slowness spectra median. Bins are 0.5dB wide.

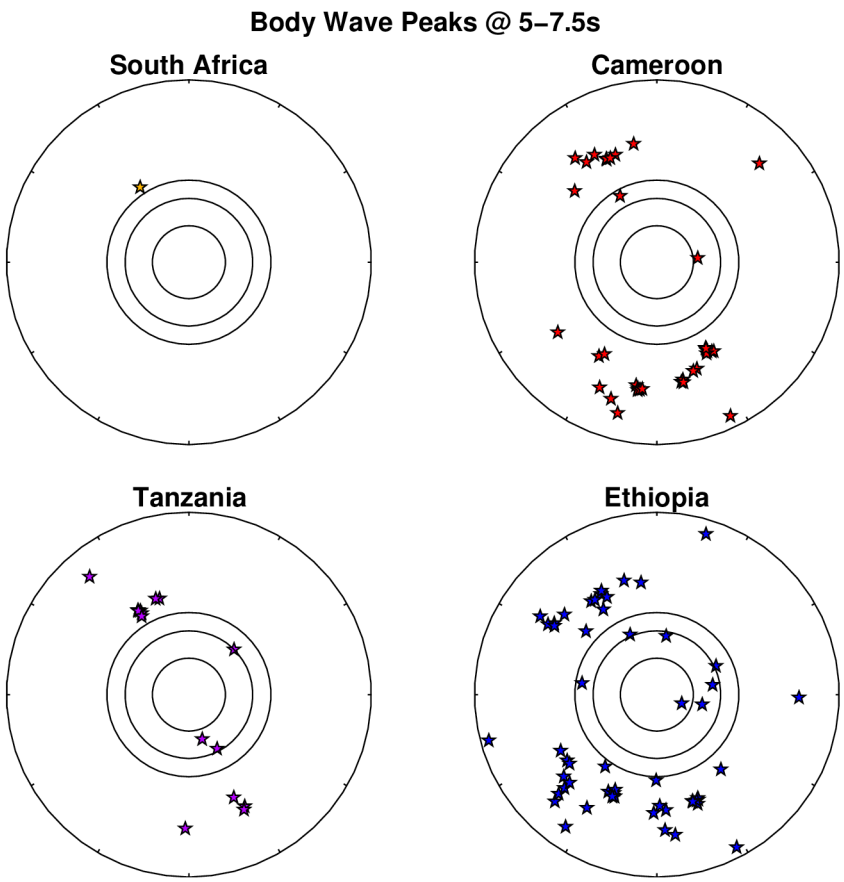

Figure 10a. All peak picks (colored stars) of each array for the 5-7.5s period range plotted in slowness space. Concentric black rings denote seismic phase ranges from Figure 3. Star coloring corresponds to that of the observing array from Figure 1.

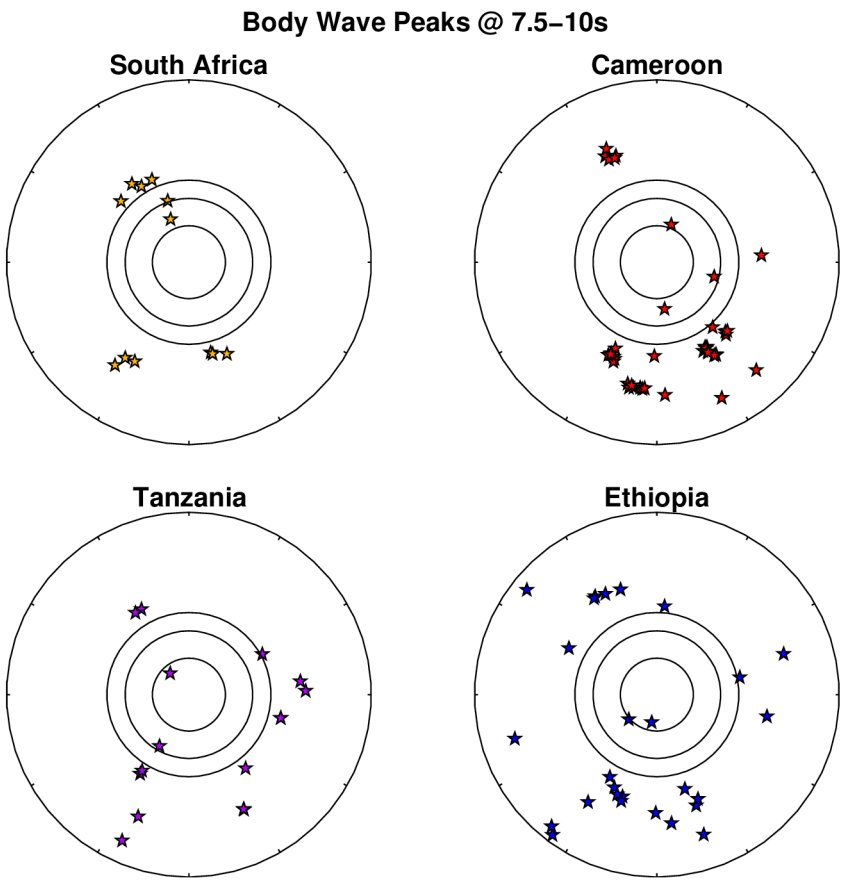

Figure 10b. Same as Figure 10a but for the 7.5-10s period range.

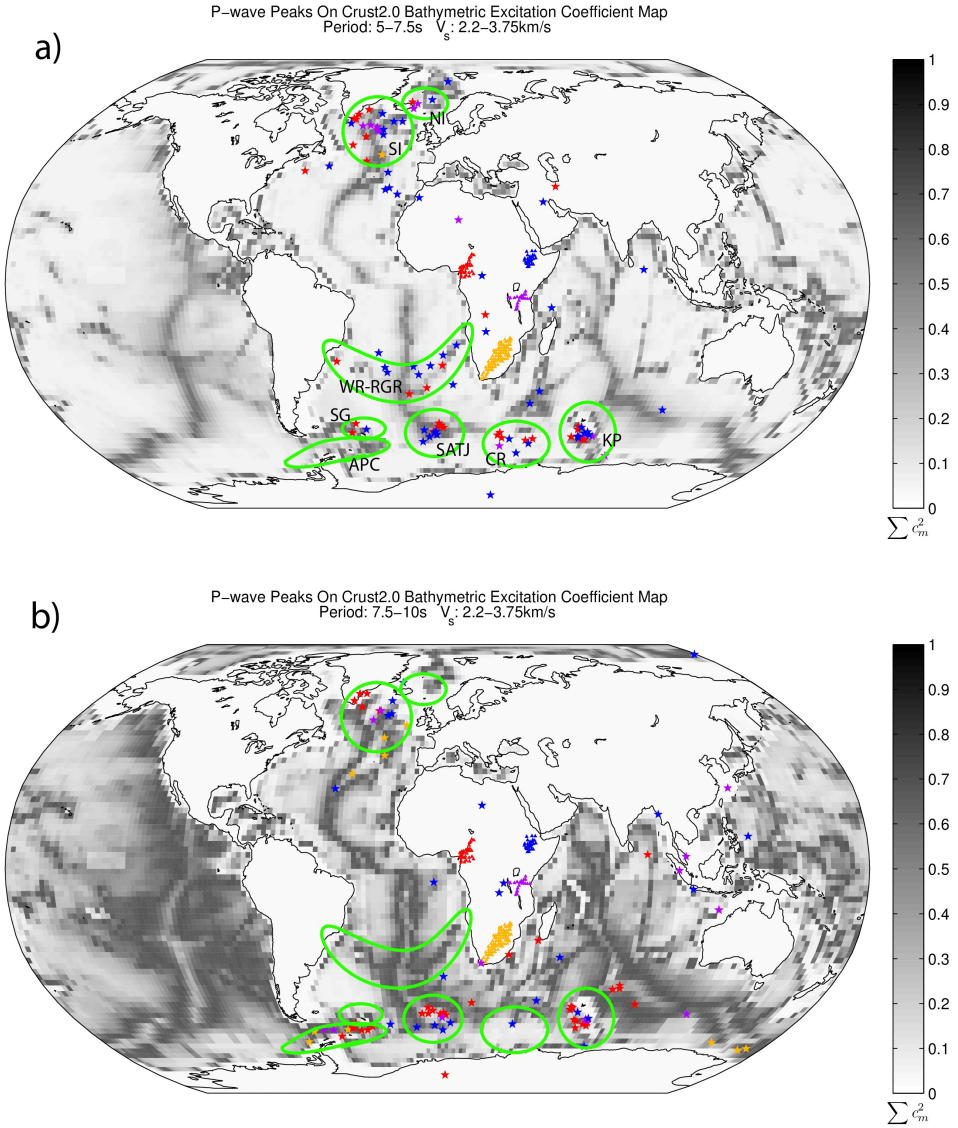

Figure 11. Backprojection of all peak picks (colored stars) from (a) Figure 10a and (b) Figure 10b in the P-wave slowness range plotted on the combined bathymetric excitation of wave-wave interference [Longuet-Higgins 1950] for Crust2.0 [Bassin et al., 2000]. Star coloring corresponds to that of the observing array (triangles). Regions outlined in green denote the main body wave microseism source locations: north of Iceland (NI), south of Iceland (SI), Walvis Ridge – Rio Grande Rise (WR-RGR), South Georgia Island (SG), Antarctic Peninsula coast (APC), South Atlantic triple junction (SATJ), Conrad Rise (CR), and Kerguluen Plateau (KP).

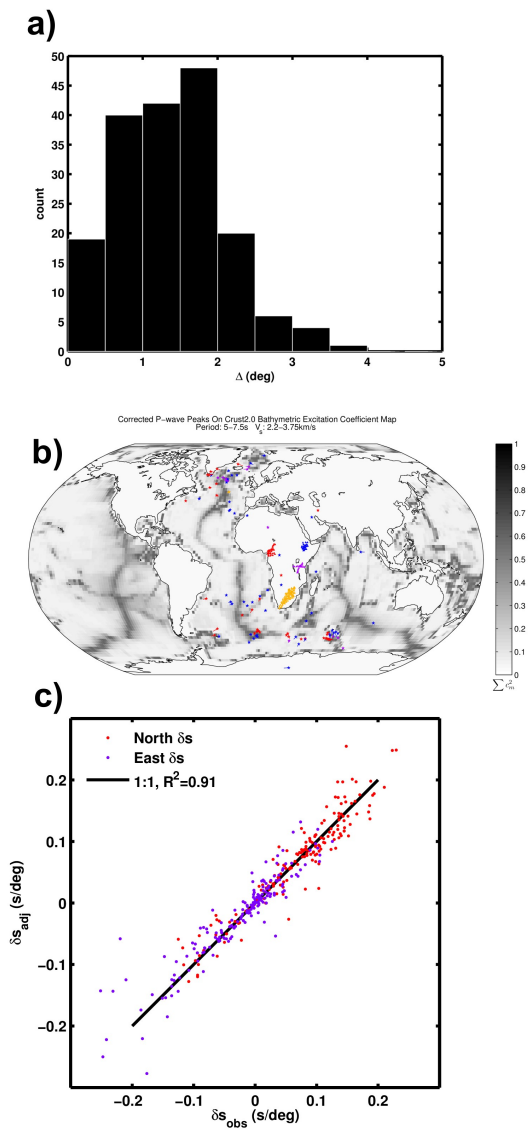

Figure 12. Correction of backprojected peak picks for 3D seismic velocity heterogeniety by accounting for crustal [Bassin et al., 2000] and mantle structure [Houser et al., 2008]. (a) Histogram for all peaks in the P-wave slowness range binned by the distance between the uncorrected source location and the source location accounting for 3D seismic velocity heterogeniety. (b) Map of the corrected peak pick locations (colored stars) and the correction vectors (lines extend to the uncorrected locations. (c) Comparison of the slowness bias caused by 3D seismic velocity heterogeniety for the uncorrected (x-axis) and corrected (y-axis) locations.

	5 – 7.5s	7.5 – 10s
Cameroon	41	38
Ethiopia	27	56
South Africa	12	1
Tanzania	16	15
Total	96	110

Table 1. Peak pick totals by array and period range.

	Jan	Feb	Mar	Apr	May	Jun	Jul	Aug	Sep	Oct	Nov	Dec	Total
North	12	9	3	2	0	0	4	1	1	1	9	8	50
South	7	8	10	11	10	12	14	9	11	10	9	6	117

Table 2. Monthly P-wave peak pick totals for northerly (N±60º) and southerly (S±60º) azimuths.